The Mousterian loess sequence La Combette (France) and its chronological framework: A re-investigation

Sebastian Kreutzer, Hélène Valladas, Pierre-Jean Texier, Virginie Moineau, Carlo Mologni, Norbert Mercier

comptes rendus palevol

2021 • 20 • 14

The Mousterian loess sequence La Combette (France) and its chronological framework: A re-investigation

Sebastian KREUTZER, Hélène VALLADAS, Pierre-Jean TEXIER, Virginie MOINEAU, Carlo MOLOGNI & Norbert MERCIER

art. 20 (14) — Published on 7 April 2021
www.cr-palevol.fr

PUBLICATIONS SCIENTIFIQUES

Couverture / *Cover* :
La fouille de La Combette, 2002 (crédits : Pierre-Jean Texier)/The La Combette excavation, 2002 (credits: Pierre-Jean Texier).

Comptes Rendus Palevol est indexé dans / Comptes Rendus Palevol *is indexed by:*
– Cambridge Scientific Abstracts
– Current Contents® Physical
– Chemical, and Earth Sciences®
– ISI Alerting Services®
– Geoabstracts, Geobase, Georef, Inspec, Pascal
– Science Citation Index®, Science Citation Index Expanded®
– Scopus®.

Les articles ainsi que les nouveautés nomenclaturales publiés dans *Comptes Rendus Palevol* sont référencés par / *Articles and nomenclatural novelties published in* Comptes Rendus Palevol *are registered on:*
– ZooBank® (http://zoobank.org)

Comptes Rendus Palevol est une revue en flux continu publiée par les Publications scientifiques du Muséum, Paris et l'Académie des sciences, Paris
Comptes Rendus Palevol *is a fast track journal published by the Museum Science Press, Paris and the Académie des sciences, Paris*

Les Publications scientifiques du Muséum publient aussi / *The Museum Science Press also publish:*
Adansonia, ***Geodiversitas***, ***Zoosystema***, ***Anthropozoologica***, ***European Journal of Taxonomy***, ***Naturae***, ***Cryptogamie*** **sous-sections** ***Algologie***, ***Bryologie***, ***Mycologie***.

L'Académie des sciences publie aussi / *The Académie des sciences also publishes:*
Comptes Rendus Mathématique, ***Comptes Rendus Physique***, ***Comptes Rendus Mécanique***, ***Comptes Rendus Chimie***, ***Comptes Rendus Géoscience***, ***Comptes Rendus Biologies***.

Diffusion – Publications scientifiques Muséum national d'Histoire naturelle
CP 41 – 57 rue Cuvier F-75231 Paris cedex 05 (France)
Tél. : 33 (0)1 40 79 48 05 / Fax : 33 (0)1 40 79 38 40
diff.pub@mnhn.fr / https://sciencepress.mnhn.fr

Académie des sciences, Institut de France, 23 quai de Conti, 75006 Paris.

ISSN (imprimé / *print*) : 1631-0683/ ISSN (électronique / *electronic*) : 1777-571X

The Mousterian loess sequence La Combette (France) and its chronological framework: A re-investigation

Sebastian KREUTZER
IRAMAT-CRP2A, UMR 5060, CNRS – Université Bordeaux Montaigne, 33607 Pessac Cedex (France)
and Geography & Earth Sciences, Aberystwyth University, Aberystwyth SY23 3DB, Wales (United Kingdom)
sebastian.kreutzer@aber.ac.uk (corresponding author)

Hélène VALLADAS
Laboratoire des Sciences du Climat et de l'Environnement, LSCE/IPSL, CEA-CNRS-UVSQ, Université Paris-Saclay, Gif-sur-Yvette (France)

Pierre-Jean TEXIER
Aix-Marseille Université, CNRS, Minist Culture, UMR 7269-LAMPEA, Aix-en-Provence (France)

Virginie MOINEAU
IRAMAT-CRP2A, UMR 5060, CNRS – Université Bordeaux Montaigne, 33607 Pessac Cedex (France)

Carlo MOLOGNI
Université Côte d'Azur, CNRS, Observatoire de la Côte d'Azur, IRD, Géoazur, 06905 Sophia Antipolis (France)

Norbert MERCIER
IRAMAT-CRP2A, UMR 5060, CNRS – Université Bordeaux Montaigne, 33607 Pessac Cedex (France)

Submitted on 26 September 2019 | Accepted on 31 March 2020 | Published on 7 April 2021

urn:lsid:zoobank.org:pub:86F0E710-F674-43A5-ABFA-F86BA2BF8D9E

Kreutzer S., Valladas H., Texier P.-J., Moineau V., Mologni C. & Mercier N. 2021. — The Mousterian loess sequence La Combette (France) and its chronological framework: A re-investigation. *Comptes Rendus Palevol* 20 (14): 225-252. https://doi.org/10.5852/cr-palevol2021v20a14

ABSTRACT
The La Combette rock-shelter, located in the Luberon mountains (Southern France), is an essential local archaeological discovery. The site comprises several Palaeolithic layers suggesting multiple phases of Mousterian occupation. The sediment sequence of *c.* 7 m thickness indicates rapid changes in the environmental conditions, which led to an abandonment of the site. While the first chronological studies were carried out in the late 1990s, in 2014, new sediment samples were taken for state-of-the-art luminescence-dating analyses using fine grain (4-11 µm) quartz and polymineral separates. Samples were taken from the loess-dominated upper archaeological levels A to D (upper main unit) as well as from the anthropogenic layer E, embedded in a fluvial context, and from the bottom deposits of the layer F/G. Here we present the obtained chronological dataset in conjunction with 24 so far unpublished thermoluminescence dating results from burnt flint artefacts from layers E and F/G. We combine and discuss our results against previous chronological datasets, which seem to be broadly confirmed by our new findings framing the sedimentation history of La Combette at 78.3 ka to 39.4 ka. In summary, it appears that the local environmental conditions were deeply impacted by the climatic changes during MIS 4/3. This caused rapid sediment influx that finally rendered the rock shelter uninhabitable as a potential refuge, until its re-discovery in the second half of the 20th century.

KEY WORDS
La Combette,
Mousterian,
chronology,
flint,
loess,
luminescence dating.

RÉSUMÉ
Une réévaluation : la séquence moustérienne loessique de La Combette et son cadre chronologique.
L'abri sous roche de La Combette, situé dans le Massif du Luberon (Sud de la France), constitue une découverte archéologique locale de toute première importance. Le site comprend plusieurs couches paléolithiques suggérant de multiples phases d'occupation moustérienne. La séquence sédimentaire, d'environ 7 m d'épaisseur, indique des dépôts de courte durée liés aux changements environnementaux saisonniers. Alors que de premières études chronologiques avaient été effectuées à la fin des années 1990, de nouveaux échantillons de sédiments ont été prélevés en 2014 et des analyses mettant en œuvre les approches les plus actuelles des méthodes de la luminescence ont été appliquées à des grains fins de quartz (4-11 µm) et à des extraits polyminéraux. Les échantillons ont été prélevés dans les niveaux archéologiques supérieurs A à D, situés en contexte loessique (unité principale supérieure), dans la couche E, associée à des dépôts fluviatiles, et dans le niveau de base F/G, caractérisé par des processus sédimentaires de versant. Nous présentons ici l'ensemble des données chronologiques ainsi que 24 résultats de datation par thermoluminescence, non publiés à ce jour, obtenus à partir d'artefacts de silex brûlés provenant des couches E et F/G. Nous combinons et discutons nos résultats par rapport aux données chronologiques déjà disponibles, qui semblent être largement confirmées, fixant ainsi le cadre temporel de l'évolution de la sédimentation à La Combette entre 78,3 ka et 39,4 ka. En résumé, il apparaît que les conditions environnementales locales ont été profondément affectées par les changements climatiques liées à l'installation du MIS 4/3. L'afflux rapide de sédiments a finalement rendu l'abri inutilisable comme refuge potentiel, jusqu'à sa redécouverte dans la seconde moitié du xxe siècle.

MOTS CLÉS
La Combette,
Moustérien,
chronologie,
silex,
loess,
datation par
luminescence.

INTRODUCTION

The proper understanding of emergence and disappearance of Neanderthals require good temporal and spatial control. The chronological framework of the Mousterian technocomplex (e.g. Bordes 1961) is of particular interest to deciphering the trajectory of the European Middle and Upper Palaeolithic. The occurrence and later disappearance of Mousterian culture and its causes have stirred lasting debates (e.g. Marshack 1989; Mellars 2004; Finlayson *et al.* 2006; Banks *et al.* 2008; Carrión & Walker 2019) within its temporal framework in Europe ranging from 350 ka (cf. Carrión & Walker 2019) to *c.* 40 ka (41.03-39.26 ka cal. BP; Higham *et al.* 2014).

Here, our study aims at adding another piece to the Neanderthals' chronology puzzle, re-evaluating old and employing new trapped charged dating results to re-investigate the chronological framework of the Mousterian site of La Combette (Texier *et al.* 1996). La Combette (Fig. 1; 43°48.45'N, 5°20.2'E) is located in the southern part of the Vaucluse Mountains ("Massif du Luberon") in South-East France. Mousterian occupation in the region was first mentioned at the very beginning of the 20th century, supported by lithic findings in the rock-shelter of Bau de l'Aubesier (Fig. 1.; Moulin 1904). Later work attributed the lithic assemblages of various further sites discovered in the region to the "typical Mousterian" (cf. overview in Buisson-Catil 2004). Those early studies used relative temporal classifications, corresponding to the bio- and pedo-stratigraphic setting, to place the regional Mousterian occupation period mainly in the last glacial/interglacial cycle.

The rock- shelter La Combette (Fig. 1) was discovered in 1973 and excavated between 1986 and 2002 (Texier *et al.* 2002; Buisson-Catil 2004). A first numerical chronology was based on four polymineral fine grain (4-11 µm) loess-dominated sediment samples using infra-red stimulated luminescence (IRSL; Hütt *et al.* 1988) in conjunction with

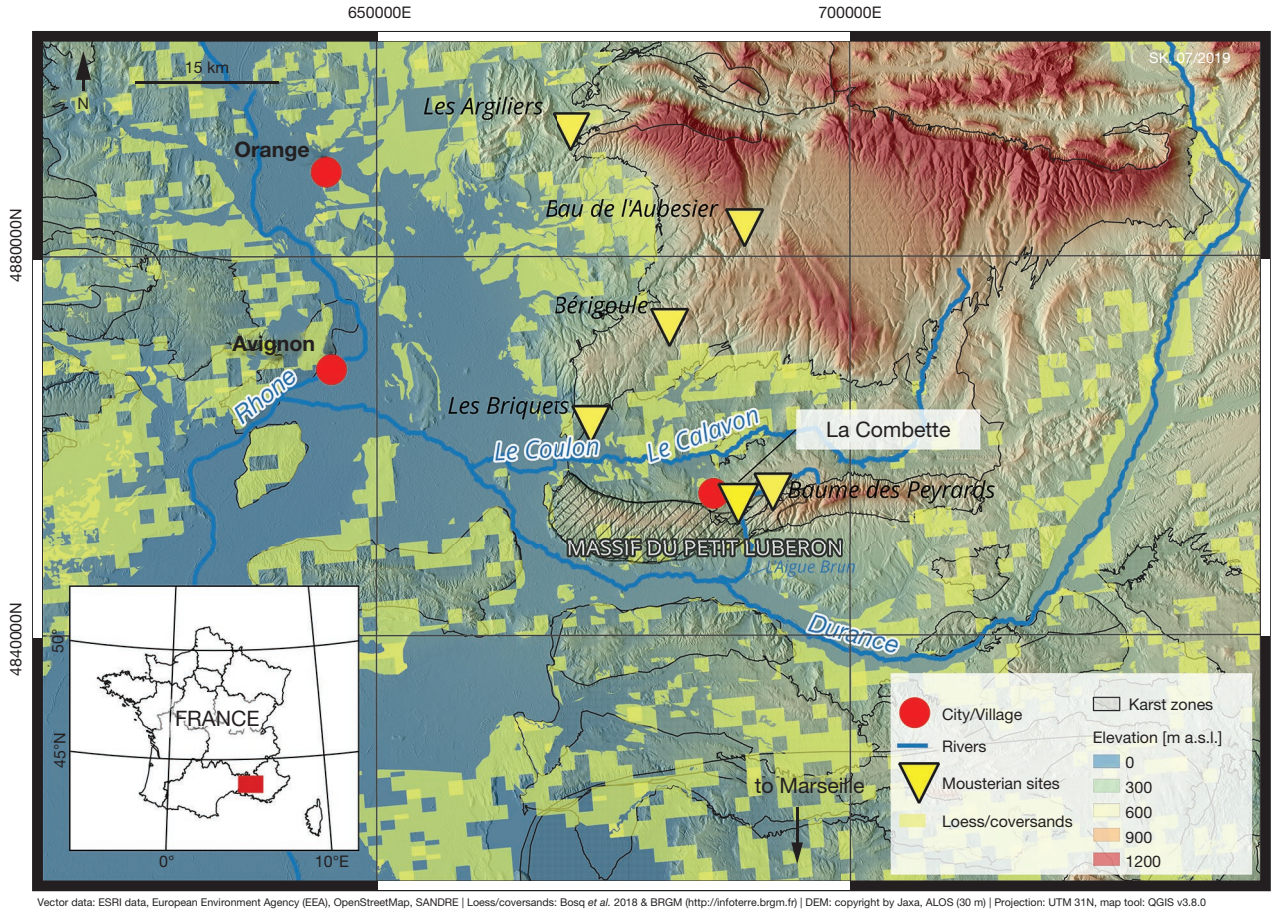

Fig. 1. — Map marking the location of La Combette at the northern foothill of the "massif du petit Luberon" along with other Palaeolithic sites in its vicinity. Areas with known loess and coversand deposits in the region are marked in yellow (data based on Bosq *et al.* 2018 and BRGM, http://infoterre.brgm.fr).

the multiple aliquot additive dose (MAAD) technique (e.g. Lang & Wagner 1996). Additionally, electron spin resonance (ESR) dating (see Rink 1997 for a review and Walther & Zilles 1994 for details on the method applied at La Combette) was applied to three heated sandstone fragments. The samples were taken in 1992 by Günther Wagner and Rolf Walther (Walther 1995; Wagner *et al.* 2002) from the archaeological layer C (cf. Fig. 2). The four sediment samples showed overlapping ages and encompassed a period between *c.* 57 ka and *c.* 64 ka (Wagner *et al.* 2002; reported data corrected for stratigraphic order), placing layer C of La Combette into the marine isotope stage (MIS) 4 (MIS boundaries in this manuscript follow Lisiecki & Raymo 2005). From the three sandstone samples, taken from a prehistoric fireplace at the bottom of layer C, only one sample (SN16; Walther 1995) showed a reasonable ESR signal with an age of 185 ± 40 ka (MIS 7 to MIS 6). Wagner *et al.* (2002) recognised the age as "surprisingly" old but reasoned that it does not contradict the "more recent knowledge" of the beginning of the Middle Palaeolithic (see also Walther 1995). Thermoluminescence (TL; Aitken 1985) measurements of heated lithic artefacts (flint) accompanied the excavation, but until 1999 only a few sufficiently heated (>450°C) flint fragments were found. This situation changed with the excavation of layer D, and in total, 24 flint samples were found suitable for TL measurements. Nevertheless, until now, neither the IRSL results nor the TL ages of the flint were formally published. Texier *et al.* (2003) and Texier (2004a, b) included the temporal range indicated by these preliminary results but did not further present or discuss details on the dating method or controversial findings.

In May 2014, six new sediment samples were taken from layers A to F/G for new luminescence measurements at the IRAMAT-CRP2A. The sampling aimed at applying modern luminescence dating methods to test the hypothesis of whether the lower archaeological layers (D to F/G) must be placed into the MIS 6/7 as proposed by Walther (1995). In the following, we present the new dating results along with the 24 so far unpublished TL ages of burnt flints and combine and discuss these findings with recalculated ages by Wagner *et al.* (2002).

Please note: Throughout our manuscript, we use "ka" (without BP or "cal.") as an abbreviation for "thousand years" when quoting luminescence ages, hence the reference year is the year of our manuscript (see discussion in Duller 2011).

STUDY SITE, THE LA COMBETTE ROCK-SHELTER (Fig. 2)

The rock-shelter is located in a Miocene molasse (Burdigalian molasse) layer at an altitude of *c.* 327 m along the Aiguebrun (l'Aigue Brun) river between the eastern flank of the "Petit Luberon" and the western flank of the "Grand Luberon" mountain ranges (Fig. 1). In the prehistoric past, it may have sheltered a potential control point along this natural passage through the Luberon mountains (Texier *et al.* 2002). Peri-Mediterranean karst formations dominate the surrounding landscape, which was not glaciated or exposed to continuous permafrost during the MIS 4-2 (Mercier 2013). With a surface of only *c.* 60 m², the rock-shelter is rather small and was completely sealed with sediment until the moment of its discovery in 1971 (Texier *et al.* 2003). Within the sediment sequence of *c.* 7 m, Texier *et al.* (2003) identified three sedimentary units and five principal archaeological layers (Fig. 2): 1) the base layer (F/G - the lower silt series), consisting of fine-sand slope deposits on the top of the bedrock with blocks and large gravels, shows first traces of multiple Mousterian occupations, e.g. in the form of intense fires (Théry-Parisot & Texier 2006); 2) layer E (embedded in fluvial sediments) is considered another important Mousterian occupation layer (Texier *et al.* 2003) with preserved charcoal and flint pieces embedded in silt and ash. Secondary loess ("loess-like" sediments) dominates the upper series, encompassing the layers: 3) D; 4) B/C; and 5) A, on top of the "Mousterian living floor" (Texier *et al.* 2003: 81). The palynological study by López-Sáez *et al.* (1998), below level F/G, revealed three palynological phases matching Würm glaciation (MIS 5d to MIS 2; cf. Ehlers *et al.* 2011) vegetation patterns.

Recently, three new parallel studies (Mologni 2017; Audiard *et al.* 2019, Mologni *et al.* submitted) supplemented the understanding of the environmental setting of La Combette. The work by Audiard *et al.* (2019) aimed at explaining the correlation between Neanderthal occupations of La Combette in view of the climatic conditions, while Mologni (2017) and Mologni *et al.* (in press) added a sedimentological and micromorphological study to understand better the sedimentary formation processes of the sequence and the related environmental conditions. Mologni (2017) and Mologni *et al.* (in press) re-classified the section into four main and twenty subunits. The lower units (their units 20 to 17) are dominated by local highly affected slope gravity-induced deposits on the top (their units 18-17) by cryogenic features (corresponding to archaeological layers F/G; Texier *et al.* 2003). Above (unit 15 upwards, Mologni *et al.* in press), the proceeding alluvial sedimentation is later interrupted (unit 8) by a reduction of the local hydrological activity and slight freeze-thaw features (Mologni *et al.* in press), corresponding to archaeological layer E in Texier *et al.* 2003). A considerable torrential event (unit 7) suggests a rapid reprise of humid conditions, followed by an abrupt transition to aeolian sedimentation patterns (units 5 to 2; corresponding to archaeological layers D, B/C, A; Texier *et al.* 2003). The loess-like sediments are believed to be of non-local origin. Relevant for this study is the secondary calcium carbonate concentration of *c.* 30% for the loessic upper part of the profile. Mologni *et al.* (in press) attributed changed climate conditions (cold and humid to cold and dry) to the observed pattern. In summary, the sequence indicates a rapid infilling of the rock-shelter (high sedimentation rate) in the upper part of the profile and with it, the presumed end of the occupation period due to changed climatic conditions.

In the context of this study, it is worth mentioning that sampling locations of our sediment samples are not the same for the lower part of the profile re-examined by Mologni *et al.* (in press). In particular, the sediment samples for our study were taken from the northern part of the profile (sector L18; fig. 6 in Texier *et al.* 2003). Although the overall sedimentation pattern applies to the six new luminescence samples taken in 2014, we performed additional granulometric analyses (Appendices 1-4) including end-member modelling using the R (R Core Team 2019) package "EMMAGeo" (Dietze *et al.* 2012; Dietze & Dietze 2019a; v0.9.6: b). Wind and water were the main geomorphic agents in control of the sediment accumulation at La Combette at the sampled locations. The upper four samples (BDX16811–BDX16814; Fig. 2; Appendix 4), composed of a mixture of silty sand and sandy silt, show a bi-modal end-member mixture, which confirmed the reworking of the original aeolian material ("loess-like" sediments). Figure 1 indicates nearby patches of loess and coversands in the north of La Combette. Those areas may have served as a source for the silty sand blown through the valley by strong North winds. In the lower part of the profile (BDX16815 and BDX16816), end-member scores indicate fluvial transport and deposition partly governed by the hillslope hydrology. Large gravels and pebbles reflect bed and traction loads, for which aeolian transport is too feeble, and large intermixing of sediments, which is consistent with the observations by Mologni *et al.* (in press).

MATERIAL AND METHODS

Our chronology builds on three datasets: 1) six sediment samples taken in 2014 and measured at the IRAMAT-CRP2A in Bordeaux; 2) 24 flint samples excavated between 1992-2002 and measured at the LSCE/IPSL in Gif-sur-Yvette; and 3) four sediment samples and one rock sample compiled in Wagner *et al.* (2002) and their ages recalculated for this study.

ABBREVIATIONS

ESR	electron spin resonance;
IRSL	infra-red stimulated luminescence;
ka	thousand years;
MAAD	multiple-aliquot additive-dose;
MIS	marine isotope stage;
TL	thermoluminescence.

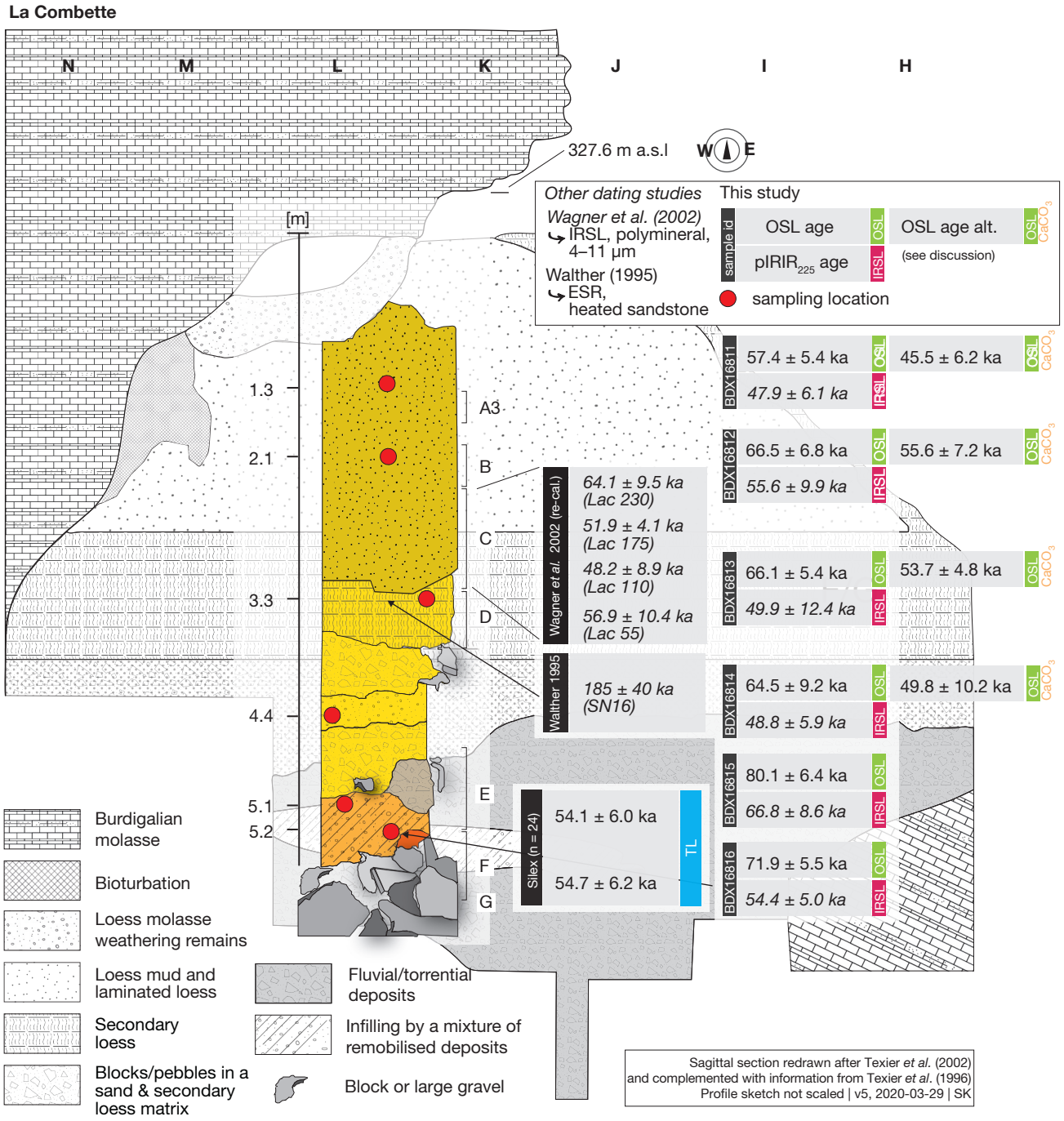

Fig. 2. — Sagittal section of the site La Combette (W to E) with the profile sampled in the framework of this study displayed on top; redrawn from Texier *et al.* (2002) and completed with information from Texier *et al.* (1996). The **red circles** indicate the OSL sampling positions. The age labels combine all ages available for La Combette. Ages labelled with "$CaCO_3$" refer to an optional modelling (cf. Discussion). See main text for details.

Sediments: OSL/post-IR IRSL dating

The sediment samples were taken at night and collected in opaque bags. The sample preparation followed standard procedures for preparing the quartz and the polymineral fine-grain (4-11 µm) fraction (cf. Preusser *et al.* 2008). This included chemical treatments with HCl, H_2O_2 and H_2SiF_6 (six days; only the quartz fraction). The fine-grain fraction was separated by applying Stokes' law. After etching, the quartz fraction was tested for potential feldspar contamination using IRSL. For the luminescence measurements (quartz, polymineral), *c.* 1 mg/aliquot of sample material was settled on stainless steel cups.

Luminescence measurements were carried out on a Freiberg Instruments Lexsyg SMART TL/OSL reader (Richter *et al.* 2015) equipped with a $^{90}Sr/^{90}Y$ β-source (dose rate *c.* 9.3 Gy s^{-1} for fine grain quartz on steel cups; calibration details cf. Appendix 5). We used green LEDs (525 Δ 20 nm; 50 mW cm^{-2}) for stimulating the quartz UV signal measured through a Schott BG 3 (3 mm) glass filter in conjunction with

TABLE 1. — List of dated burnt flint samples with dose rates, equivalent dose and age values.

Sample	Square	Field ID	Layer	Depth [m]	Year	$\dot{D}_{total}$ [Gy ka^{-1}]	D_e [Gy]	Age [ka]
LC01	J12	34	E	4.8	1994	0.49 ± 0.03	31.19 ± 0.55	64.2 ± 5.6
LC03	J12	–	E	4.8	1994	0.40 ± 0.03	25.97 ± 3.45	64.2 ± 9.1
LC04	J14	160	F/G	5.5	1997	1.11 ± 0.08	59.81 ± 3.30	54.0 ± 6.0
LC05	I13	173	F/G	5.71	1997	1.00 ± 0.05	48.92 ± 2.59	49.0 ± 4.1
LC07	J13	193	F/G	5.62	1997	1.05 ± 0.06	61.46 ± 4.71	58.7 ± 5.7
LC08	I13	114	F/G	5.51	1997	1.43 ± 0.08	69.34 ± 2.74	48.6 ± 4.4
LC09	L14	127	E	4.67	1997	0.63 ± 0.05	30.23 ± 3.07	48.1 ± 5.9
LC12	J17	490	E	4.48	1999	0.76 ± 0.03	42.80 ± 6.10	56.2 ± 7.4
lC15	K13	129	F/G	5.52	1999	0.61 ± 0.05	33.50 ± 1.20	55.2 ± 5.2
LC16	L12	676	F/G	6.07	1999	2.40 ± 0.20	134.00 ± 1.50	55.9 ± 7.2
LC17	M16	247	E	4.48	1999	0.80 ± 0.03	42.80 ± 1.00	53.4 ± 3.5
LC19	N16	144	E	4.35	1999	2.01 ± 0.13	108.80 ± 4.10	54.1 ± 5.5
LC21	J12	617	F/G	5.87	2000	0.86 ± 0.05	40.00 ± 1.30	46.5 ± 3.6
LC22	K12	613	F/G	5.79	2000	0.95 ± 0.05	58.50 ± 2.80	61.3 ± 5.1
LC23	I12	157	F/G	5.59	2000	1.03 ± 0.14	56.40 ± 1.00	54.5 ± 8.2
LC24	I18	294	E	4.3	2000	1.08 ± 0.06	58.40 ± 1.30	54.3 ± 4.4
LC25	N17	118	E	4.34	2000	0.55 ± 0.04	32.00 ± 1.00	58.4 ± 5.4
LC26	J12	382	F/G	5.66	2000	0.69 ± 0.06	35.50 ± 5.30	51.8 ± 8.7
LC27	N17	121	E	4.33	2000	1.28 ± 0.07	58.40 ± 2.00	45.6 ± 4.0
LC28	I18	79	E	4.16	2000	1.93 ± 0.08	103.80 ± 2.30	53.9 ± 4.8
LC29	J12	527	F/G	5.84	2000	0.90 ± 0.09	62.10 ± 1.50	69.3 ± 8.7
LC30	K12	301	F/G	5.61	1999	0.86 ± 0.06	47.20 ± 1.10	54.9 ± 4.7
LC31	N17	257	E	4.47	2000	1.52 ± 0.06	70.00 ± 1.60	46.1 ± 3.8
LC32	N17	169	E	4.42	2000	2.21 ± 0.14	119.00 ± 2.30	53.9 ± 5.3

a Delta 365/50 EX interference filter in front of a Hamamatsu H7360-02 photomultiplier tube. The blue-violet signal emitted by feldspars in the polymineral fraction was stimulated with infrared LEDs (820 Δ 20 nm; 120 mW cm^{-2}) and detected through a filter set consisting of a Schott BG 39 (3 mm) and an AHF-BL HC 414/46 interference filter.

For measuring the quartz fraction, we applied the single aliquot regenerative (SAR) dose protocol after Murray & Wintle (2000). The post-IR IRSL protocol (Thomsen *et al.* 2008) at 225°C (cf. Buylaert *et al.* 2009), henceforth pIRIR$_{225}$, was used for measuring the polymineral fraction. For full details on the applied protocol settings and measurement conditions, we refer readers to the supplement (Appendix 5).

BURNT FLINTS: THERMOLUMINESCENCE (TL) DATING (Table 1)

Twenty-four burnt flint artefacts (cf. Table 1) were prepared and measured in the Gif-sur-Yvette laboratory. All samples showed burning features on their surface, indicating a heating of the artefacts before burial. Each sample was first cut with a diamond saw to remove the outer rim (>2 mm), affected by external α- and β-particles. In a second step, the remaining parts were crushed in an agate mortar and sieved to obtain 100-160 µm grains. Subsequent washing in HCl ensured the removal of contaminating carbonates. The 100-160 µm grains were used for TL experiments, but a fraction was subsequently crushed to obtain fine grains (4-11 µm) used for α-efficiency (S_α) determination. These fine grains were first heated at 500°C for erasing any TL signal and then deposited on stainless steel discs. Half of the discs we irradiated with α-particles (^{238}Pu source delivering 2.255 × 10^6 α-particles s^{-1} cm^{-2}) while the second half was β-irradiated with a ^{90}Sr/^{90}Y source (dose-rate *c.* 7.5 Gy min^{-1}). For further details on the procedure, we refer readers to Mercier *et al.* (1992).

The multiple-aliquot additive-dose (MAAD) technique was applied for determining the palaeodose. External γ-irradiation was carried out with a homemade irradiator, equipped with a ^{137}Cs source (*c.* 1.3 Gy min^{-1}, calibrated against a ^{60}Co secondary standard beam; cf. Valladas 1978; Tribolo *et al.* 2019). Sixteen aliquots (10 mg/aliquot) of each sample, which received additional γ-doses, were heated progressively to 500°C (heating rate: 5 K s^{-1}) in a homemade TL reader (Valladas *et al.* 1994). The TL signals were detected through a UV-blue (350-450 nm) filter combination.

DOSE-RATE DETERMINATION

For the sediment samples (BDX16811–BDX16816), U, Th and K concentrations were determined using high-resolution γ-ray spectrometry measurements at the IRAMAT-CRP2A. Except for sample BDX16811, the γ-dose rate was recorded by carbon-doped Al_2O_3 single crystal detectors (Akselrod *et al.* 1990) stored for six months *in situ* in the sampling position (cf. Kreutzer *et al.* 2018a for a system description). The recorded *in situ* γ-doses were measured using a Daybreak 2000 luminescence reader (Bortolot 2000) equipped with green LEDs, with a measurement protocol comparable to Kreutzer *et al.* (2018a) and corrected for the water content using values determined from the samples taken in the field. For the α-efficiency (here: *a*-value) we assumed 0.035 ± 0.005 for the quartz fraction (e.g. Lai *et al.* 2008), 0.11 ± 0.02 for the polymineral fraction (pIRIR$_{225}$; Kreutzer *et al.* 2014). For re-calculating the results by Wagner *et al.* (2002), we used the information published in the report and related to the technique in Lang & Wagner (1996). All numerical parameters can be deduced from the CSV-file provided as a supplement.

For the flint samples, the internal U, Th, K contents were measured using neutron activation analysis (NAA) (Joron

TABLE 2. — Nuclide concentrations and dose-rate values of the sediment samples. Abbreviations: **M**, mineral; **Q**, quartz; **PM**, polymineral. Values for the samples "Lac" were taken from Wagner *et al.* (2002) if quoted in italic. For all samples, a common mean water content of 5 ± 2.5% was assumed. *a*-values: quartz fraction: 0.035 ± 0.005, polymineral (this study): 0.11 ± 0.02 (Wagner *et al.* 2002; Kreutzer *et al.* 2014: IRSL MAAD). The $\dot{D}_{Al2O3:C}$ quoted results are corrected for the water content measured from the field samples due to input restrictions in DRAC (cf. Appendices) and thus express the dry dose-rate. (*) Mean ± standard deviation calculated from values obtained for BDX16812–BDX16816.

Sample	M	U [ppm]	Th [ppm]	K [%]	$\dot{D}_{\gamma Al2O3:C}$ [Gy ka^{-1}]	$\dot{D}_{int}$ [Gy ka^{-1}]	$\dot{D}_{ext}$ [Gy ka^{-1}]	$\dot{D}_{cosm.}$ [Gy ka^{-1}]	$\dot{D}_{total}$ [Gy ka^{-1}]
BDX16811	Q	1.71 ± 0.03	5.64 ± 0.07	0.91 ± 0.02	0.51 ± 0.02*	0.002 ± 0.001	2.00 ± 0.05	0.19 ± 0.02	2.00 ± 0.05
	PM					0.029 ± 0.011	2.54 ± 0.12		2.57 ± 0.12
BDX16812	Q	1.52 ± 0.03	4.65 ± 0.07	0.75 ± 0.02	0.54 ± 0.05	0.002 ± 0.001	1.79 ± 0.07	0.17 ± 0.02	1.80 ± 0.07
	PM					0.029 ± 0.011	2.25 ± 0.12		2.28 ± 0.12
BDX16813	Q	1.53 ± 0.03	5.15 ± 0.08	0.75 ± 0.02	0.51 ± 0.05	0.002 ± 0.001	1.77 ± 0.07	0.14 ± 0.01	1.77 ± 0.07
	PM					0.029 ± 0.011	2.25 ± 0.12		2.28 ± 0.12
BDX16814	Q	1.92 ± 0.29	5.64 ± 0.08	0.88 ± 0.02	0.49 ± 0.05	0.002 ± 0.001	1.94 ± 0.07	0.12 ± 0.01	1.94 ± 0.07
	PM					0.029 ± 0.011	2.51 ± 0.14		2.54 ± 0.14
BDX16815	Q	2.22 ± 0.03	2.43 ± 0.05	0.37 ± 0.06	0.52 ± 0.05	0.002 ± 0.001	1.48 ± 0.06	0.12 ± 0.01	1.48 ± 0.06
	PM					0.029 ± 0.011	1.96 ± 0.13		1.99 ± 0.13
BDX16816	Q	2.11 ± 0.03	4.70 ± 0.07	0.64 ± 0.02	0.51 ± 0.05	0.002 ± 0.001	1.76 ± 0.07	0.11 ± 0.01	1.76 ± 0.07
	PM					0.029 ± 0.011	2.32 ± 0.14		2.34 ± 0.14
Lac 55	*PM*	*1.57 ± 0.08*	*4.61 ± 0.20*	*0.71 ± 0.23*	*0.51 ± 0.02**	*0.029 ± 0.011*	*2.2 ± 0.21*	*0.15 ± 0.02*	*2.23 ± 0.21*
Lac 110	*PM*	*1.83 ± 0.15*	*5.04 ± 0.41*	*0.69 ± 0.05*	*0.51 ± 0.02**	*0.029 ± 0.011*	*2.34 ± 0.14*	*0.16 ± 0.02*	*2.37 ± 0.14*
Lac 175	*PM*	*1.75 ± 0.09*	*4.32 ± 0.19*	*0.78 ± 0.07*	*0.51 ± 0.02**	*0.029 ± 0.011*	*2.32 ± 0.13*	*0.18 ± 0.02*	*2.35 ± 0.13*
Lac 230	*PM*	*1.60 ± 0.13*	*4.49 ± 0.42*	*0.70 ± 0.05*	*0.51 ± 0.02**	*0.029 ± 0.011*	*2.23 ± 0.12*	*0.19 ± 0.02*	*2.26 ± 0.12*

1974) in the Pierre Süe laboratory (Saclay, France) and used to calculate the internal α- and β-dose rates. For determining the α-efficiency, the α- and β-irradiated discs were measured, and the corresponding TL signals (TL_α/TL_β) compared (Valladas & Valladas 1982). The γ-dose was estimated using calcium sulphate dosimeters in copper capsules located in the vicinity of the flint samples (Valladas 1985).

AGE COMPILATION AND DATA ANALYSIS

The luminescence data analysis was carried out using the R (R Core Team 2019) package 'Luminescence' (Kreutzer *et al.* 2012, 2018b). For the modelling (Fig. 7) in the discussion, we also used R in conjunction with the R packages "coda" (Plummer *et al.* 2006; v0.19-3) and 'ggplot2' (Wickham 2016; v3.2.1) for the visualisation. The Al_2O_3:C chip measurements were analysed with the self-written software Anatol (Gaugez & Mercier 2012), and for analysing the high-resolution γ-ray spectrometry results, we applied a self-written MS Excel™ sheet (unpublished). For calculating the luminescence ages, we used a modified version of the age calculator DRAC (Durcan *et al.* 2015; v1.2) running on a local server. This customised DRAC version accounts for the higher calcium carbonate concentration of the sediment by adjusting the water correction factors using information from Nathan & Mauz (2008) and Kreutzer *et al.* (2019a) (see supplement for details). The applied settings and the full DRAC output table are provided as supplements (Appendices 4; 15; 16).

RESULTS

DOSE-RATE DETERMINATION (Table 2)

Table 2 summarizes the results of the high-resolution γ-ray spectrometry and the γ-dose rates measured with the Al_2O_3:C dosimeters for the samples taken in 2014. Across the sediment samples, the mean concentration varies between 1.5 ppm and 2.2 ppm for U, between 2.4 ppm to 5.6 ppm for Th, and 0.4% to 0.9% for K. Sample BDX16815 always showed the lowest values. We detected no radioactive disequilibria in the U decay chain. Table 2 also lists the dosimetric values from Wagner *et al.* (2002) for the matter of completeness. Assumed internal U and Th concentrations followed Vandenberghe *et al.* (2008) (U: 0.08 ± 0.02 ppm; Th: 0.180 ± 0.03 ppm) for the quartz fraction. The internal K concentration for the polymineral fraction was assumed to be 10 ± 2%. Smedley *et al.* (2012) considered this value being more realistic for single-grain K-feldspar than the 12.5 ± 0.5% suggested by Huntley & Baril (1997). For our study, we assumed that the majority of the luminescence IRSL and $pIRIR_{225}$ signals was dominated by K-feldspar grains in the polymineral fraction. In summary, the environmental-dose rate varies on average between 1.5-2.0 Gy ka^{-1} for the fine-grain quartz fraction and 2.0-2.6 Gy ka^{-1} for the polymineral fine-grain fraction. These values are in good agreement with the re-calculated values for the polymineral fine-grain fraction (2.3-2.4 Gy ka^{-1}) deduced from the dating study by Wagner *et al.* (2002).

For samples BDX16812–BDX16816, the environmental γ-dose rates were measured with passive dosimeters ($\dot{D}_{\gamma\_Al2O3:C}$) range from 0.49 Gy ka^{-1} to 0.54 Gy ka^{-1} with a mean ± standard deviation of 0.51 ± 0.02 Gy ka^{-1}. These values are consistent with the 0.48 ± 0.16 Gy ka^{-1} reported by Walther (1995) (*in situ* measurement, moisture corrected *c.* 0.51 Gy ka^{-1}). In comparison, for sample BDX16811, where no passive dosimeter could be used and $\dot{D}_\gamma$ was not measured *in situ* but was derived from U, Th, and K concentrations, this $\dot{D}_\gamma$ is higher by *c.* 34% than the average $\dot{D}_\gamma$ derived from the Al_2O_3:C dosimeters. Given the large homogeneity of the measured *in situ* $\dot{D}_\gamma$ values, we decided to calculate a central *in situ* $\dot{D}_\gamma$. Hence, a value of 0.51 ± 0.02 Gy ka^{-1} was applied to all samples for which no *in situ* measurement data were available. This value was also

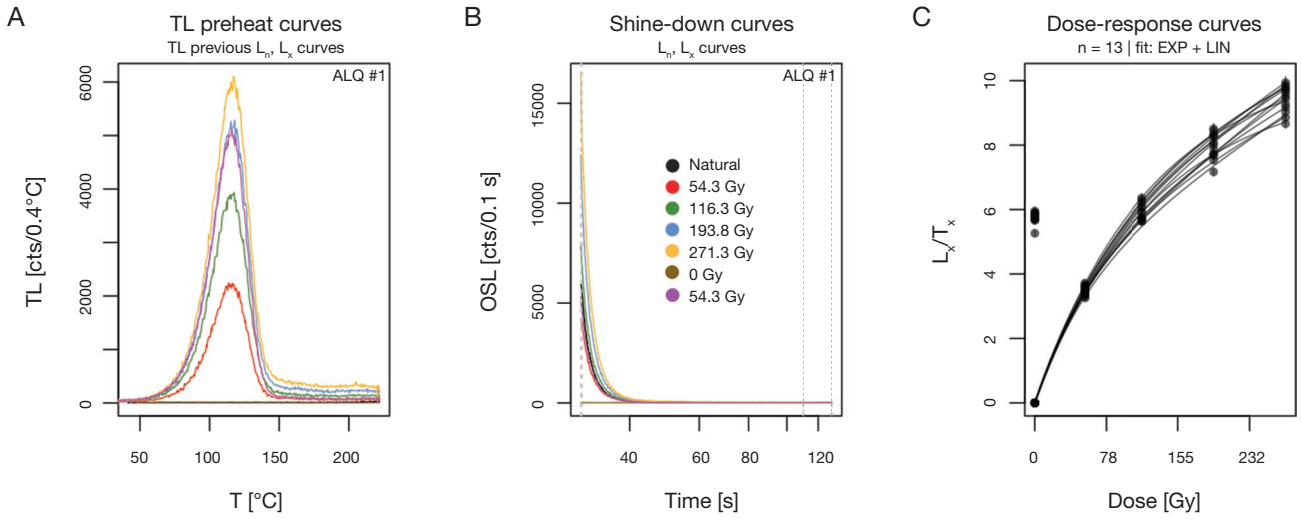

FIG. 3. — Exemple of TL preheat curves (**A**), OSL shine-down curves (**B**), and (**C**) combined dose-response curves for sample BDX16812 (quartz). All curves indicate a bright and reproducible luminescence signal.

used to recalculate the dataset by Wagner *et al.* (2002). We display different $\dot{D}_\gamma$ calculation scenarios in Appendix 14; the effect on the final age distribution is negligible.

For the flint samples, the dose rate is dominated (>50%) by α and β-particles originating from internal U, Th, and K concentrations which we assumed to be homogeneously distributed. However, the concentration may vary spatially over one artefact and significantly from specimen to specimen (e.g. Schmidt *et al.* 2012) where high U concentrations (>3 ppm) likely indicate hotspots prone to dose-rate overestimations (e.g. Selo *et al.* 2009). We found internal radio-element concentrations that vary significantly between the 24 samples (U: 1.2 ± 1.1 ppm, Th: 0.1 ± 0.1 ppm, K: 0.03 ± 0.02%). The average *in situ* environmental dose rate was estimated at 1.1 ± 0.6 Gy ka^{-1} (mean ± standard deviation). The external $\dot{D}_\gamma$ over all samples is 0.4 ± 0.1 Gy ka^{-1}. This value is a little bit lower than the average $\dot{D}_\gamma$ measured with the Al_2O_3:C chips for the sediment sample; however, it overlaps within uncertainties. The obtained S_α values averages at 20.1 ± 5.0 µGy/(10^{3}α cm^{-2}) and are consistent with measurements of other burnt flint samples (e.g. Mercier *et al.* 1991; Richter *et al.* 2007).

SEDIMENTS: GREEN-OSL/POST-IR IRSL DATING

Fine grain quartz green-OSL (Fig. 3)

In Figure 3A-C, we display typical preheat TL curves, green OSL shine-down curves, and dose-response curves for the fine grain quartz sample BDX16812. Figure 3A, B show curves from the first aliquot, while Figure 3C combines all 13 measured dose-response curves of the sample combined in one plot. The presented (as well as the not presented) curves appear typical for green-OSL curves. All showed a sufficiently bright (non-noised) luminescence signal with reproducible 110°C peaks (Fig. 3A) and comparable dose-response curve shapes (Fig. 3C). We selected a preheat / cutheat temperature combination of 220°C (preheat) and 180°C (cutheat) based on preheat-plateau tests and preheat-dose-recovery tests on two (BDX6811, BDX16814) and four samples (BDX16811-BDX16814) respectively (Appendix 9A, B). In retrospective, it appears that a preheat / cutheat combination of 240°C/180°C might have been the slightly better choice. However, we wanted to avoid a potential dose overestimation observed for sample BDX16813 (Appendix 9B), and the results are consistent within error margins. In the dose-recovery tests, indicating a meaningful selection of measurement protocol parameters (Appendix 9B), BDX16811 appeared as an outlier against the other samples. However, for this sample, we also observed shine-down curves very different from the OSL curves of the other samples (data not shown). After re-etching the samples for another three days in H_2SiF_6 (after the performed preheat dose-recovery test), all curves look similar to the curves of the other samples. We presume that the odd signal was caused by a carbonate crust around the grains, which was removed after the etching, and we, therefore, adapted the preheat / cutheat temperature combination as stated above.

Figure 4 shows the equivalent dose (D_e) distributions for the six measured quartz samples (tabulated results in Table 3). The coefficient of variation (c_v) is smaller than 10% for all samples except BDX16814. For the samples BDX16813, BDX16815, and BDX16816, c_v is smaller than 5%. In Table 3 we quoted the arithmetic average ± standard deviation for each sample. Over the entire profile, the averaged equivalent doses overlap within uncertainties for all samples.

The fine-grain green-OSL quartz ages are listed in Table 3 and Figure 2. The ages increase with depth from [52.0-62.8] ka (BDX16811) at the top of the profile to *c.* [66.4-77.4] ka (BDX16816) at the bottom of the profile. Samples BDX16813, BDX16814 and BDX16816, seem to indicate a slight age inversion. However, all ages overlap within 2-sigma and are thus statistically indistinguishable.

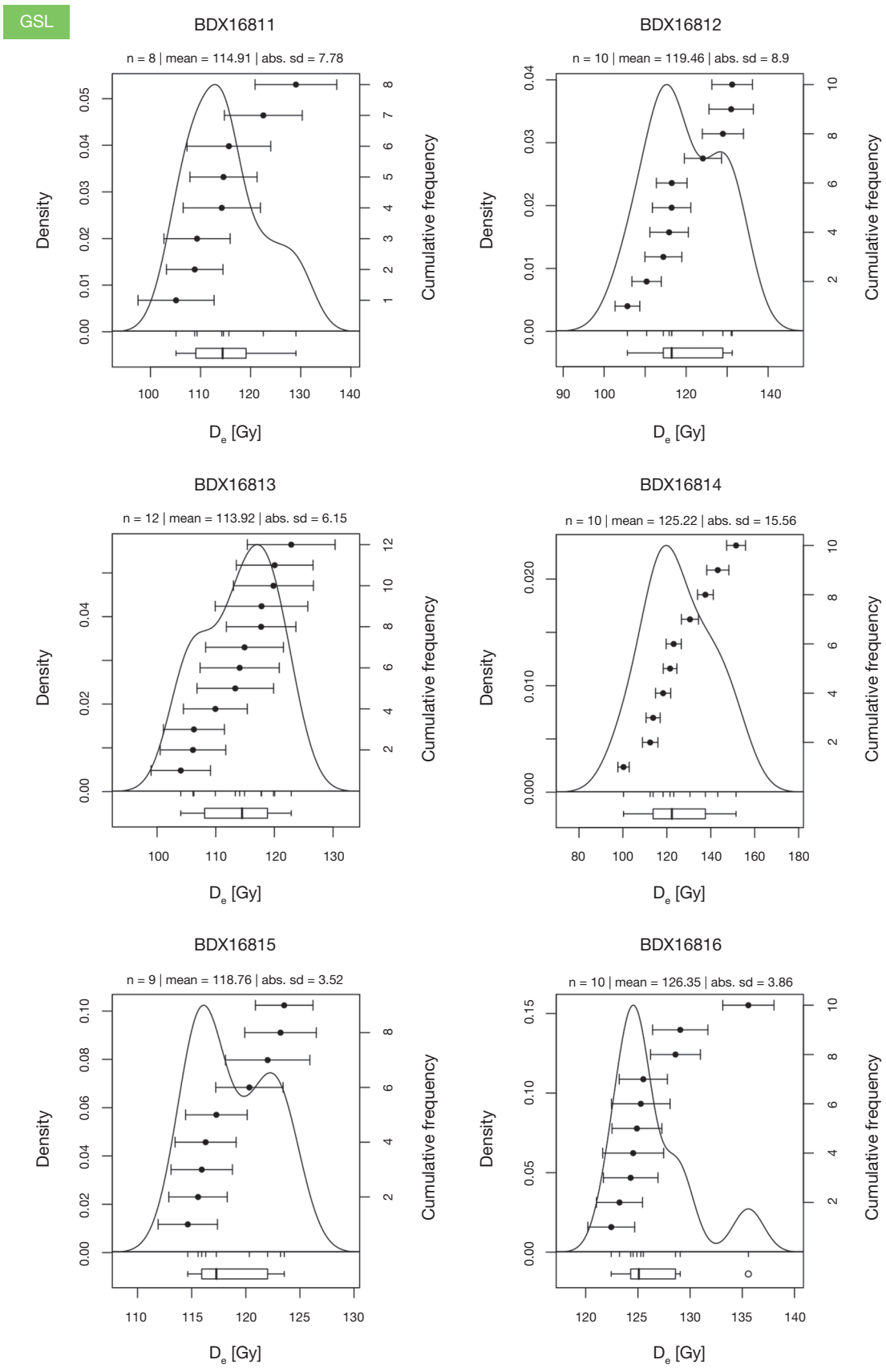

FIG. 4. — Kernel density plots showing the D_e distributions (fine grain quartz) for all measured samples. Similar plots for the $pIRIR_{225}$ measurements can be found in Appendix 10.

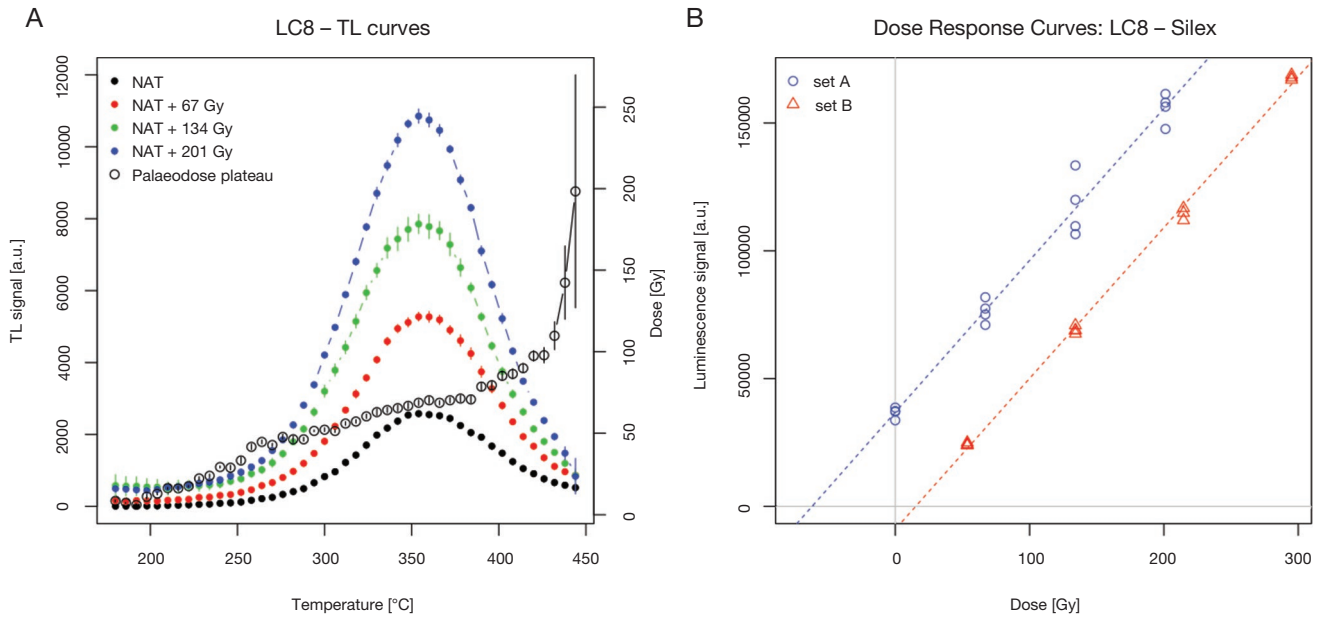

FIG. 5. — **A**, typical additive TL curves showing the luminescence characteristics of the flint sample LC8 and the palaeodose plateau. All peaks proved reproducible with no visible peak shift; **B**, dose-response curves for a set of natural + added doses (set **A**, **blue**) and regenerated doses (set **B**, **red**).

TABLE 3. — Equivalent doses and luminescence ages. Abbreviations: **M**, mineral; **Q**, quartz; **PM**, polymineral; **N**, number of accepted aliquots / total number of measured aliquots.

Sample	M	Protocol	N	FIT	$\dot{D}_{total}$ [Gy ka^{-1}]	D_e [Gy]	Age [ka]
BDX16811	Q	GSL-SAR	8/14	EXP+LIN	2 ± 0.1	114.9 ± 7.8	57.4 ± 5.4
	PM	pIRIR$_{225}$	3/3	EXP	2.6 ± 0.1	122.8 ± 12.4	47.9 ± 6.1
BDX16812	Q	GSL-SAR	10/13	EXP+LIN	1.8 ± 0.1	119.5 ± 8.9	66.5 ± 6.8
	PM	pIRIR$_{225}$	3/3	EXP	2.3 ± 0.1	127 ± 20.4	55.6 ± 9.9
BDX16813	Q	GSL-SAR	13/13	EXP+LIN	1.8 ± 0.1	117.2 ± 4.8	66.1 ± 5.4
	PM	pIRIR$_{225}$	3/3	EXP	2.3 ± 0.1	114 ± 26.8	49.9 ± 12.4
BDX16814	Q	GSL-SAR	10/10	EXP+LIN	1.9 ± 0.1	125.2 ± 15.6	64.5 ± 9.2
	PM	pIRIR$_{225}$	3/3	EXP	2.5 ± 0.1	123.9 ± 11.2	48.8 ± 5.9
BDX16815	Q	GSL-SAR	9/9	EXP+LIN	1.5 ± 0.1	118.8 ± 3.5	80.1 ± 6.4
	PM	pIRIR$_{225}$	23/23	EXP	2 ± 0.1	132.6 ± 12.3	66.8 ± 8.6
BDX16816	Q	GSL-SAR	10/10	EXP+LIN	1.8 ± 0.1	126.4 ± 3.9	71.9 ± 5.5
	PM	pIRIR$_{225}$	29/29	EXP	2.3 ± 0.1	127.6 ± 4.9	54.4 ± 5.0
Lac 55	*PM*	*IRSL MAAD*	*20*	*LIN*	*2.2 ± 0.2*	*127 ± 20*	*56.9 ± 10.4*
Lac 110	*PM*	*IRSL MAAD*	*20*	*LIN*	*2.4 ± 0.1*	*114 ± 20*	*48.2 ± 8.9*
Lac 175	*PM*	*IRSL MAAD*	*20*	*LIN*	*2.4 ± 0.1*	*122 ± 7*	*51.9 ± 4.1*
Lac 230	*PM*	*IRSL MAAD*	*20*	*LIN*	*2.3 ± 0.1*	*145 ± 20*	*64.1 ± 9.5*

Polymineral fine-grain pIRIR$_{225}$

Initially, following the old age expectation by Walther (1995), we separated and measured the polymineral fine-grain fraction. Equivalent doses exceeding 125 Gy may lay in the UV signal saturation range of quartz OSL (e.g. Roberts 2008) and would have resulted in minimum age estimates for the quartz fraction only. The D_e distributions for all polymineral fine grain samples are given in the supplement (Appendix 10). For samples BDX16811-BDX16814, we measured only three aliquots each, while for samples BDX16815-BDX16816, 23 respectively 29 aliquots were measured. Except for sample BDX16816 at the bottom of the profile, the D_e scatter is equal or even exceeds 10%; however, with overlapping error bars. Corresponding ages are shown in Figure 2 and are listed in Table 3. All quoted pIRIR$_{225}$ polymineral fine-grain ages are systematically younger than the ages from the quartz separates. When measuring the polymineral fine grain fraction, pIRIR$_{225}$ measurements target the feldspar separates known to suffer from so-called anomalous fading (Wintle 1973), i.e., an unwanted single loss leading to age underestimation. Correction methods such as suggested by Huntley & Lamothe (2001) can be employed but would need additional measurements to estimate the fading rate which was not employed for this study after the quartz fraction was found to provide ages which appeared to be reliable. Therefore, in Figure 2, pIRIR$_{225}$ are quoted in italic letters. However, the performed pIRIR$_{225}$ measurements

provide two crucial information. The bleaching rate of the $pIRIR_{225}$ is considerably slower than for quartz OSL (e.g. Thomsen *et al.* 2008). Thus, the younger ages imply that the signal resetting of the quartz fraction was sufficient. Furthermore, the two ages at the bottom of the profile do not indicate an age beyond the saturation limit of the quartz fraction.

Burnt flint TL dating (Fig. 5)

Figure 5 shows typical TL curves (here sample LC8) with a reproducible dose-response of the peak around 360°C to 380°C in the wavelength range 350 nm to 450 nm. For all the flints from La Combette, since only a single peak was present at high temperature (*c.* 380°C), no preheat was applied before the signal measurement.

In Table 1, we summarized basic numerical information for each investigated flint sample (full details in Appendix 11). Although D_es range from 26 Gy (LC3) to 134 Gy (LC16), the corresponding ages are statistically indistinguishable. Figure 6 shows the age distributions for burnt flint samples from archaeological layer E (black circles) and the lower layer F/G (red triangles). The grey polygon in the so-called Abanico plot (Dietze *et al.* 2016) marks the two-sigma range of the standard estimates. All samples from both layers fall within this range. In other words, the results likely belong to one joint distribution of ages, reflected by the age ranges (68% confidence interval) of [48.1-60.1] ka for artefacts from layer E vs [48.5-60.1] ka for layer F/G.

These findings allow us to combine our results, for each layer, in an isochron plot where the slope of the regression line is a function of the D_e values and internal dose rates only (Appendix 12). The corresponding isochron ages differ slightly from the mean ages of the layers (more for samples from layer E: 49.1 ± 2 ka) but overlap within 2-sigma error margins, confirming our common external dose and age assumptions. The figure might be further interpreted as evidence of our homogenous radionuclide distribution assumption (section Dose-rate determination) since we would not expect to observe all values sitting along one line if radioactive hotspots led to dose-rate overestimations.

DISCUSSION

We started our investigation to test the hypothesis proposed by Walther (1995) that the archaeological layers below C belong to MIS 6/7 and with this, perhaps represent a much older Mousterian occupation period. Neither the lower quartz OSL ages nor the $pIRIR_{225}$ nor the TL ages from the lithic artefacts (Fig. 2) indicate ages that may date older than the late MIS 5. Hence, an obvious outcome of our study is the rejection of the hypothesis by Walther (1995, based on a single ESR age) of an early Mousterian occupation preserved in the lower archaeological layers. Beyond this rather clear finding, our investigations contain a couple of loose ends we are going to tie up in following.

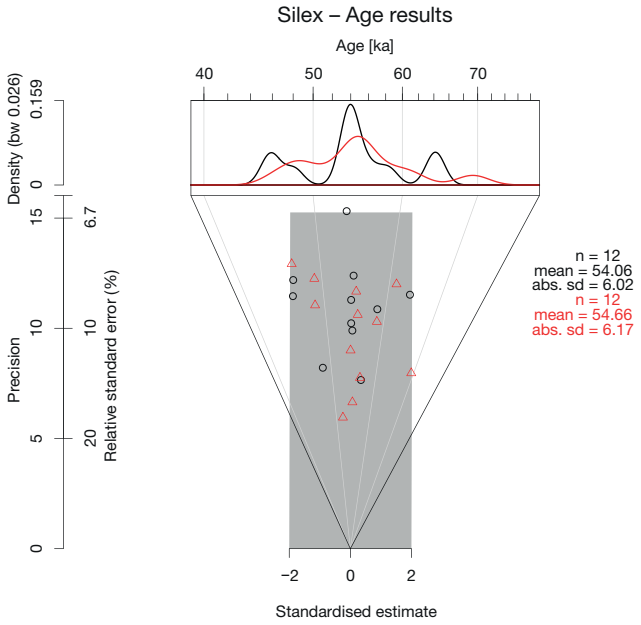

Fig. 6. — Abanico plot (Dietze *et al.* 2016) showing the age distribution of all measured flint samples from the archaeological layers E (**black**) and F/G (**red**). Plotted are standardised ages values against their precision. The upper x-axis displays the corresponding ages in ka. All ages are lying within 2-sigma (**grey polygon**) around a common age, i.e. the ages are statistically indistinguishable.

Chronological subtleties

If the uppermost sample (BDX16811) would have been calculated using U, Th, and K concentrations for the $\dot{D}_\gamma$ the corresponding age would be 53.2 ± 5.0 ka instead of 57.4 ± 5.4 ka and still overlap within 2-sigma uncertainties with the other samples. For this particular sample, we could not measure the *in situ* γ-dose rate which, for all other five OSL samples, varied significantly from values derived by high-resolution γ-ray spectrometry in comparison to the *in situ* values (*c.* 34%). In contrast to *in situ* measurements, γ-dose rates determined based on laboratory experiments rely on the assumption that the sampled and then the analysed material (*c.* 100 g) best represents the field situation. In particular, it makes an important assumption on the sediment's homogeneity regarding the distribution of the radionuclides. The observed differences between γ-dose rates obtained with the two methods indicate a heterogenous radionuclide distribution. Therefore, leaving severe measurement errors as an alternative possibility aside, we believe that the *in situ* measurements best represent the environmental situation. Our choice is further supported by the rather low γ-dose rates obtained by the calcium sulphate dosimeters. The alternative age of BDX16811 ($\dot{D}_\gamma$ derived from U, Th, and K values) can be considered as a possible minimum age.

We did not perform further measurements (e.g. fading, unbleachable residual) on the polymineral fine-grain fraction measured with $pIRIR_{225}$. Such measurements are time-consuming and error-prone (e.g. Kadereit *et al.* 2020; at the same time, we consider the possibility that the lowermost sample would result in an age older than MIS 5 negligible. Moreover, the $pIRIR_{225}$ results gave sufficient evidence that

the sediment was exposed to sunlight long enough to reset the $pIRIR_{225}$ signal and thus the signal of the quartz fraction.

Surprising is the OSL quartz dataset in light of the TL ages from the 24 burned lithic (flint) artefacts. First, as written above, all TL ages appear to originate from a single age distribution, thus despite the widely differing D_e values, they are highly consistent and reproducible. Second, the ages are systematically younger than one would expect from the stratigraphic position in the lower part of the profile below BDX16811-BDX16814. The two lower OSL quartz ages (BDX16815 and BDX16816) are unproblematic given the average based age inversion (BDX16815 vs BDX16816) and the setting in a disturbed part of the profile. Table 1 lists the depth of the artefacts as found at La Combette.

In contrast to the laterally fixed sampling position for the six new luminescence samples in 2014, the flint samples were spread over the surface of the archaeological layers. In other words, Figure 2 is a simplified summary of the stratigraphical setting, and we believe that the OSL ages of BDX16815 and BDX16816 are in stratigraphic order with the flint ages. Similarly, the age inversion of BDX16815 instead reflects an unfortunate sampling position in a small sand-filled channel (see also end-member modelling in Appendix 4) with older sediment.

However, such interpretation does not hold for the encountered age inversion between the OSL quartz and the flint ages. The sediment is well stratified, and well above the stratigraphic position of the archaeological layers E and F/G, and the burnt flint results do not seem to give any reason for suspicions. Layers E and F/G show a high calcium carbonate concentration of detrital origin up to 70% (Mologni *et al.* in press). Nathan & Mauz (2008) reported on dose-rate modelling in carbonate-rich environments subject to secondary cementation processes and showed that, if not accounted for, carbonate cementation can lead to either over- or underestimation of age due to altered dose rates over time. The setting, in particular marine environments, reported by Nathan & Mauz (2008), is, however, not similar to La Combette. Nevertheless, Mologni *et al.* (in press) reported secondary carbonate (*c.* 30%) in the upper part of the profile, which may lead to a comparable situation, as reported by Nathan & Mauz (2008). We, therefore, applied the R package 'RCarb' (Kreutzer *et al.* 2019a), an implementation of the initial work by Nathan & Mauz (2008), in R, to the upper four samples of La Combette. For the modelling, we assumed that the cementation process sets on around 15 ka ago (with the end of MIS 2) and ended at 5 ka. The initial water content was set to 15 ± 5% (final as reported above), the $CaCO_3$ concentration was set to 40 ± 10% for all four samples based on Mologni *et al.* (submitted) (see supplement for all CSV-file with all input and output values, used R code: Appendix 5). The new modelling-based OSL quartz ages are displayed in Figure 2 (graphical output 'RCarb': Appendix 13). If our carbonate cementation assumption is valid, all upper four samples, also the samples by Wagner *et al.* (2002), which were not tested though, would shift toward younger ages becoming on average stratigraphically (more) consistent with the TL flint ages. Although the onset and the finalisation of the cementation has a minor impact on the accuracy of the modelling (e.g. Mauz & Hoffmann 2014), the initial assumption that the sediment was affected by cementation processes with similar effects to the dose-rate as reported by Nathan & Mauz (2008) remains questionable and could not be resolved for our study. Hence, our carbonate modelling represents another possible scenario with very large uncertainties.

A contradictory scenario caused by radionuclide heterogeneities (cf. section Dose-rate determination) in the specimen may render all flint ages too young, leaving only the green-OSL ages valid. The data at hand (section Burnt flint TL dating; Appendix 12) in conjunction with the high calcium carbonate concentration observed at La Combette, however, do not favour such a scenario. Nevertheless, the scenario cannot be excluded, but to test it, further extensive analyses to detail the microcrystalline structure and the spatial distribution of radionuclides (e.g. Selo *et al.* 2009; Schmidt *et al.* 2012, 2013) would have been needed, which was beyond available resources for our study. Moreover, as mentioned above, such a scenario would have led to dots not aligned in the isochron plots (Appendix 12), which is contrary to what we observed.

Finally, a conclusive chronology?

With all the data and options at hand, it leaves the question of how final can our comprehensive dataset be? The first, crucial observation is that the polymineral IRSL ages presented by Wagner *et al.* (2002) and recalculated for our study still fit into our new chronology, although they show considerable uncertainties and age inversions. In contrast to the $pIRIR_{225}$ ages, which appear to suffer from athermal fading, this does not seem to be the case for Wagner's dataset: they reported "[…] after a storage time of six months, non-significant signal loss was observed." (Wagner *et al.* 2002: 109). The measurement technique (MAAD, e.g. Lang & Wagner 1996) applied to multiple aliquots of a sample to construct a dose-response curve including long pause and preheat times differs from the currently preferred single aliquot approach with shorter measurement times. Nevertheless, a detailed discussion of the potential reasons for this observation is beyond the scope of our manuscript. In summary, we consider all flint ages, the dataset by Wagner *et al.* (2002) as well as our OSL fine grain quartz ages, valid in the sense that they are compatible with a single chronostratigraphic model (see below).

Figure 7 displays all three age datasets ordered by depth. The archaeological layers are colour-coded next to the y-axis; additional MIS boundaries ease the temporal placements. To constrain the time-span of the infilling of La Combette, which might be related to the occupation period, we used a re-sampling approach based on parametric bootstrapping. 10^6 random ages were drawn from normal distributions defined by the mean and standard deviation of each sample. Their layer classification pooled these age datasets, e.g. all random ages from layer F/G represent one new dataset. From these sets, we sampled another 10^6 ages with replacement. The results exhibit a kernel density plot (Fig. 7; below the central plot) with 68% and 95% probability density intervals

illustrated. Based on this modelling, the site was most likely filled between [78.3-39.4] ka, i.e., between MIS 5a and the end of MIS 3. This interval, may or may not render the exact Mousterian occupation period. In the absence of other datable assemblages, the data do not exclude the possibility that the site was used before the MIS 5a, although that appears to be an unlikely scenario (see also data in López-Sáez *et al.* 1998). Chronostratigraphic, sedimentological and palaeoclimatological comparisons to local-to-regional sedimentary archives proposed by Mologni *et al.* (in press) suggests a slightly earlier infilling of the rock-shelter during MIS 5b/5a.

While the beginning of the Mousterian occupation must remain vague, the rapid sediment influx within *c.* 10 ka in the late MIS 3 determines its end and aligns with our current understanding of changed climate conditions during this period (e.g. Obreht *et al.* 2017). This period, however, still represents several hundred Mousterian generations (e.g. Carrión & Walker 2019).

In addition to Figure 7, we modelled the infilling period with the ages corrected for possible carbonate cementation process (Appendix 14). The results are primarily comparable to Figure 7, but shift the margins slightly by *c.* 1.5 ka towards younger ages. Our approach can be further modified by pooling all ages from one archaeological layer and making an additional assumption on the distribution, i.e., reducing the weights of layers with more ages. However, we found that this does not correctly reflect our data. Besides, the differing number of dates per layer slightly biases our approach shown in Figure 7 and its classification by the archaeological layer and not, e.g. the depth.

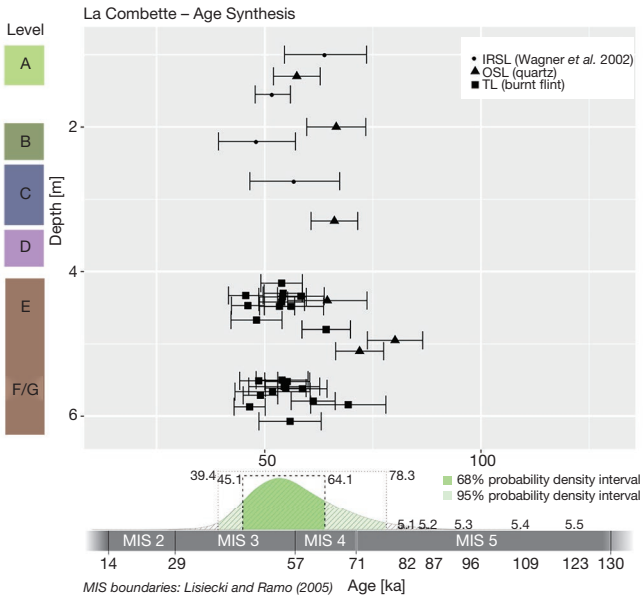

Fig. 7. — Age synthesis plot with results from Wagner *et al.* (2002) and this study (fine grain quartz OSL and burnt flints). Shown are ages against the profile depth. Error bars indicate 1-sigma uncertainties. Archaeological layers are coloured coded. We assigned similar colours to layer E and F/G since the transition between these layers appears a little bit fuzzy. Below the main plot, a kernel density plot, based on level-wise resampling from the probability distributions, shows the likely occupation period of the site (see Discussion).

The spatial-temporal setting of La Combette in perspective

Besides its importance for the Mousterian occupation history in the region, La Combette is also a loess (dominated) sequence preserved in a rock-shelter. Loess records are valuable global terrestrial climate archives with a long research history (for Europe, e.g. Zöller & Semmel 2001; Rousseau *et al.* 2007; Zöller 2010) and the potential to track rapid climate changes (Rousseau & Sima 2014). The La Combette loess complex seems to embrace the MIS 4/3 transition (or to use the French nomenclature, the transition from the Lower to the Middle Pleniglacial; cf. Antoine *et al.* 2016) with a sedimentation rate peak in the early MIS 3. In loess records all over Europe, this period indicates substantial climate alterations (e.g. Antoine *et al.* 2009, 2016). For example, Antoine *et al.* (2013) reported a sharp layer transition in the stratigraphy before the inset of the MIS 2 loess and Meszner *et al.* (2013) even reported a hiatus between *c.* 50 ka and 30 ka before the onset of new cold-climate loess deposition. The recent work by Obreht *et al.* (2017) identified an increased intensity of the Siberian High after the Campanian Ignimbrite super-volcano eruption around 39 ka (Marti *et al.* 2016) as a possible cause for an increased migration pressure due to massive climate fluctuations. Whether this event may have played a role in the final sealing of La Combette as a refuge during the last sub-millennials or it happened significantly afterward cannot be answered. On the other hand, chronological data point to an abrupt sediment deposition at the site within *c.* 10 ka. In regard to chronological findings from other Mousterian sites, our data appear less blurred. The occupation period reported by Richter *et al.* (2007) for the Bérigoule site frames [90-54] ka. Data originating from more distant sites in France appear compatible with our findings (for recent studies also using luminescence dating techniques, e.g. La Ferrassie: Guérin *et al.* 2015, Frouin *et al.* 2017a; La Quina: Frouin *et al.* 2017b, Roc de Marsal: Guérin *et al.* 2017). Moreover, while, as mentioned above, the earlier occupation is unlikely (albeit our data do not support it), the (possible) end of the Mousterian occupation period aligns with the sizeable ^{14}C dataset by Higham *et al.* (2014) (41.03-39.26 ka cal. BP).

SUMMARY AND CONCLUSIONS

The above-presented results mark the endpoint of a chronological re-investigation we started back in 2014 and iterated over the years in poster presentations based on new data and modified assumptions. We rejected the hypothesis that the lower archaeological layers E and F/G may represent much older Mousterian occupation. Based on 24 TL burnt flint ages, six OSL quartz fine-grain ages and four IRSL polymineral fine-grain dates, the sedimentation period of the archaeological layers F/G (bottom) to A (top) spans 78.3 ka to 39.4 ka (95% probability density interval). Other sediments in the more southern part of the site, which we did not sample, might be older. With this, the (recorded) sedimentation history of La Combette began during the outgoing MIS 5a and ended

abruptly in the late MIS 3. The data suggest that the infilling of the upper part of the profile did not take longer than 10 ka and it certainly ended the occupation of the site around 39 ka, which is compatible with the current understanding of the disappearance of Neanderthals in Europe. Finally, while our results from a single site must not be overstated, our work contributes a piece helping to complete the prehistoric puzzle in France as the contact zone between Neanderthals and first modern humans in the MIS 3.

Acknowledgements
We are grateful to one anonymous reviewer for a thoughtful review. We thank Jean-Louis Joron from the Pierre Süe laboratory (Saclay, France) for the flint nuclide data using NAA and Alain Queffelec from the PACEA (University of Bordeaux) for running the grain size measurements. Thanks to Daniel Richter for reminding us on the work by Rolf Walther. The work was supported by the LaScArBx. LaScArBx is a research programme supported by the ANR (ANR-10-LABX-52).

REFERENCES

Aitken M. J. 1985. — *Thermoluminescence dating*. Academic Press, 359 p.

Aitken M. J. & Xie J. 1990. — Moisture correction for annual gamma dose. *Ancient TL* 8: 6-9.

Akselrod M. S., Kortov V. S., Kravetsky D. J. & Gotlib V. I. 1990. — Highly Sensitive Thermoluminescent Anion-Defective Alpha-Al_2O_3:C Single Crystal Detectors. *Radiation Protection Dosimetry* 32: 15-20. https://doi.org/10.1093/oxfordjournals.rpd.a080715

Antoine P., Rousseau D.-D., Moine O., Kunesch S., Hatté C., Lang A., Tissoux H. & Zöller L. 2009. — Rapid and cyclic aeolian deposition during the Last Glacial in European loess: a high-resolution record from Nussloch, Germany. *Quaternary Science Reviews* 28: 2955-2973. https://doi.org/10.1016/j.quascirev.2009.08.001

Antoine P., Rousseau D.-D., Degeai J.-P., Moine O., Lagroix F., Kreutzer S., Fuchs M., Hatté C., Gauthier C., Svoboda J. & Lisa L. 2013. — High-resolution record of the environmental response to climatic variations during the last interglacial-glacial cycle in central Europe: the loess-palaeosol sequence of Dolní Věstonice (Czech Republic). *Quaternary Science Reviews* 67: 17-38. https://doi.org/10.1016/j.quascirev.2013.01.014

Antoine P., Coutard S., Guérin G., Deschodt L., Goval E., Locht J.-L. & Paris C. 2016. — Upper Pleistocene loess-palaeosol records from northern France in the European context: Environmental background and dating of the Middle Palaeolithic. *Quaternary International* 411: 4-24. https://doi.org/10.1016/j.quaint.2015.11.036

Armitage S. J. & Bailey R. M. 2005. — The measured dependence of laboratory beta dose rates on sample grain size. *Radiation Measurements* 39: 123-127. https://doi.org/10.1016/j.radmeas.2004.06.008.

Audiard B., Thery-Parisot I., Blasco T., Mologni C., Texier P.-J. & Battipaglia G. 2019. — Crossing taxonomic and isotopic approaches in charcoal analyses to reveal past climates. New perpectives in paleobotany from the Palaeolithic Neanderthal dwelling-site of La Combette (Vaucluse, France). *Review of Palaeobotany and Palynology* 266: 52-60. https://doi.org/10.1016/j.revpalbo.2019.04.002

Banks W. E., d'Errico F., Peterson A. T., Kageyama M., Sima A. & Sánchez-Goñi M.-F. 2008. — Neanderthal Extinction by Competitive Exclusion. *PLOS ONE* 3: e3972-8. https://doi.org/10.1371/journal.pone.0003972

Bordes F. 1961. — Mousterian Cultures in France: Artifacts from recent excavation dispel some popular misconceptions about Neanderthal man. *Science* 134: 803-810. https://doi.org/10.1126/science.134.3482.803

Bortolot V. J. 2000. — A new modular high capacity OSL reader system. *Radiation Measurements* 32: 751-757. https://doi.org/10.1016/S1350-4487(00)00038-X

Bosq M., Bertran P., Degeai J.-P., Kreutzer S., Queffelec A., Moine O. & Morin E. 2018. — Last Glacial aeolian landforms and deposits in the Rhône Valley (SE France): Spatial distribution and grain-size characterization. *Geomorphology* 318: 1-20. https://doi.org/10.1016/j.geomorph.2018.06.010

Brennan B. J., Lyons R. G. & Phillips S. W. 1991. — Attenuation of alpha particle track dose for spherical grains. *International Journal of Radiation Applications and Instrumentation. Part D. Nuclear Tracks and Radiation Measurements* 18 (1-2): 249-253. https://doi.org/10.1016/1359-0189(91)90119-3

Buisson-Catil J. 2004. — Le Paléolithique moyen en Vaucluse : Historique des Recherches, *in* Barthélémy A. (ed.), *Vaucluse Préhistorique : Le territoire, Les hommes, les cultures et les sites*. Ministère de la Culture et de la Communication, Le Pontet: 53-60.

Buylaert J. P., Murray A. S., Thomsen K. J. & Jain M. 2009. — Testing the potential of an elevated temperature IRSL signal from K-feldspar. *Radiation Measurements* 44: 560-565. https://doi.org/10.1016/j.radmeas.2009.02.007

Carrión J. S. & Walker M. J. 2019. — Background to Neanderthal presence in western Mediterranean Europe. *Quaternary Science Reviews* 217: 7-44. https://doi.org/10.1016/j.quascirev.2018.10.011

Dietze E. & Dietze M. 2019a. — Grain-size distribution unmixing using the R package EMMAgeo. *E&G Quaternary Science Journal* 68: 29-46. https://doi.org/10.5194/egqsj-68-29-2019

Dietze M. & Dietze E. 2019b. — EMMAgeo: End-Member Modelling of Grain-Size Data. *CRAN* version 0.9.6. Available at: https://CRAN.R-project.org/package=EMMAgeo.

Dietze E., Hartmann K., Diekmann B., IJmker J., Lehmkuhl F., Opitz S., Stauch G., Wünnemann B. & Borchers A. 2012. — An end-member algorithm for deciphering modern detrital processes from lake sediments of Lake Donggi Cona, NE Tibetan Plateau, China. *Sedimentary Geology* 243-244: 169-180. https://doi.org/10.1016/j.sedgeo.2011.09.014

Dietze M., Kreutzer S., Burow C., Fuchs M. C., Fischer M. & Schmidt C. 2016. — The abanico plot: visualising chronometric data with individual standard errors. *Quaternary Geochronology* 31: 12-18. https://doi.org/10.1016/j.quageo.2015.09.003

Duller G. A. T. 2011. — What date is it? Should there be an agreed datum for luminescence ages? *Ancient TL* 29: 1-4.

Durcan J. A., King G. E. & Duller G. A. T. 2015. — DRAC: Dose Rate and Age Calculator for trapped charge dating. *Quaternary Geochronology* 28: 54-61. https://doi.org/10.1016/j.quageo.2015.03.012

Ehlers J., Gibbard P. L. & Hughes P. D. 2011. — *Quaternary Glaciations - Extent and Chronology*, 1st ed. Elsevier, pp. 1126 p.

Finlayson C., Giles Pacheco F., Rodríguez-Vidal J., Fa D. A., María Gutierrez López J., Santiago Pérez A., Finlayson G., Allue E., Baena Preysler J., Cáceres I., Carrión J. S., Fernández Jalvo Y., Gleed-Owen C. P., Jimenez Espejo F. J., López P., Antonio López Sáez J., Antonio Riquelme Cantal J., Sánchez MarcoA., Giles Guzman F., Brown K., Fuentes N., Valarino C. A., Villalpando A., Stringer C. B., Martinez Ruiz F. & Sakamoto T. 2006. — Late survival of Neanderthals at the southernmost extreme of Europe. *Nature* 443: 850-853. https://doi.org/10.1038/nature05195

FROUIN M., GUÉRIN G., LAHAYE C., MERCIER N., HUOT S., ALDEIAS V., BRUXELLES L., CHIOTTI L., DIBBLE H. L., GOLDBERG P., MADELAINE S., MCPHERRON S. J. P., SANDGATHE D., STEELE T. E. & TURQ A. 2017a. — New luminescence dating results based on polymineral fine grains from the Middle and Upper Palaeolithic site of La Ferrassie (Dordogne, SW France). *Quaternary Geochronology* 39: 131-141. https://doi.org/10.1016/j.quageo.2017.02.009

FROUIN M., LAHAYE C., VALLADAS H., HIGHAM T., DEBÉNATH A., DELAGNES A. & MERCIER N. 2017b. — Dating the Middle Paleolithic deposits of La Quina Amont (Charente, France) using luminescence methods. *Journal of Human Evolution* 109: 30-45. https://doi.org/10.1016/j.jhevol.2017.05.002

GAUGEZ C. & MERCIER N. 2012. — Anatol (Analyse Thermo Opto Luminescence), v2.0.6 (*unpublished software*).

GILBERT E. R., DE CAMARGO M. G. & SANDRINI-NETO L. 2014. — rysgran: Grain size analysis, textural classifications and distribution of unconsolidated sediments. CRAN version 2.1.0. https://CRAN.R-project.org/package=rysgran

GUÉRIN G., MERCIER N. & ADAMIEC G. 2011. — Dose-rate conversion factors: update. *Ancient TL* 29: 5-8.

GUÉRIN G., MERCIER N., NATHAN R., ADAMIEC G. & LEFRAIS Y. 2012. — On the use of the infinite matrix assumption and associated concepts: A critical review. *Radiation Measurements* 47: 778-785. https://doi.org/10.1016/j.radmeas.2012.04.004

GUÉRIN G., FROUIN M., TALAMO S., ALDEIAS V., BRUXELLES L., CHIOTTI L., DIBBLE H. L., GOLDBERG P., HUBLIN J.-J., JAIN M., LAHAYE C., MADELAINE S., MAUREILLE B., MCPHERRON S. J. P., MERCIER N., MURRAY A. S., SANDGATHE D., STEELE T. E., THOMSEN K. J. & TURQ A. 2015. — A multi-method luminescence dating of the Palaeolithic sequence of La Ferrassie based on new excavations adjacent to the La Ferrassie 1 and 2 skeletons. *Journal of Archaeological Science* 58: 147-166. https://doi.org/10.1016/j.jas.2015.01.019

GUÉRIN G., FROUIN M., TUQUOI J., THOMSEN K. J., GOLDBERG P., ALDEIAS V., LAHAYE C., MERCIER N., GUIBERT P., JAIN M., SANDGATHE D., MCPHERRON S. J. P., TURQ A. & DIBBLE H. L. 2017. — The complementarity of luminescence dating methods illustrated on the Mousterian sequence of the Roc de Marsal: A series of reindeer-dominated, Quina Mousterian layers dated to MIS 3. *Quaternary International* 433: 102-115: https://doi.org/10.1016/j.quaint.2016.02.063

HIGHAM T., DOUKA K., WOOD R., RAMSEY C. B., BROCK F., BASELL L., CAMPS M., ARRIZABALAGA A., BAENA J., BARROSO-RUÍZ C., BERGMAN C., BOITARD C., BOSCATO P., CAPARRÓS M., CONARD N. J., DRAILY C., FROMENT A., GALVÁN B., GAMBASSINI P., GARCIA-MORENO,A., GRIMALDI S., HAESAERTS P., HOLT B., IRIARTE-CHIAPUSSO M.-J., JELINEK A., JORDÁ PARDO J. F., MAÍLLO-FERNÁNDEZ J.-M., MAROM A., MAROTO J., MENÉNDEZ M., METZ L., MORIN E., MORONI A., NEGRINO F., PANAGOPOULOU E., PERESANI M. PIRSON S., LA RASILLA, DE M., RIEL-SALVATORE J., RONCHITELLI A., SANTAMARIA D., SEMA P., SLIMAK L., SOLER J., SOLER N., VILLALUENGA A., PNHASI R. & JACOBI R. 2014. — The timing and spatiotemporal patterning of Neanderthal disappearance. *Nature* 512: 306-309. https://doi.org/10.1038/nature13621

HUNTLEY D. J. & BARIL M. R. 1997. — The K content of the K-feldspars being measured in optical dating or in the thermoluminescence dating. *Ancient TL* 15: 11-13.

HUNTLEY D. J. & LAMOTHE M. 2001. — Ubiquity of anomalous fading in K-feldspars and the measurement and correction for it in optical dating. *Canadian Journal of Earth Sciences* 38: 1093-1106. https://doi.org/10.1139/cjes-38-7-1093

HÜTT G., JAEK I. & TCHONKA J. 1988. — Optical dating: K-Feldspars optical response stimulation spectra. *Quaternary Science Reviews* 7: 381-385. https://doi.org/10.1016/0277-3791(88)90033-9

JORON J. L. 1974. — *Contribution à l'analyse des éléments en traces dans les roches et les minéraux par activation neutronique. in Application à la caractérisation d'objets archéologiques.* PhD Dissertation, Université Paris-Sud-XI, Paris.

KADEREIT A., KREUTZER S., SCHMIDT C. & DEWITT R. A. 2020. — A closer look at IRSL SAR fading data and their implication for luminescence dating. *Geochronology* Discuss. (preprint). https://doi.org/10.5194/gchron-2020-3

KREUTZER S., SCHMIDT C., FUCHS M. C., DIETZE M., FISCHER M. & FUCHS M. 2012. — Introducing an R package for luminescence dating analysis. *Ancient TL* 30: 1-8.

KREUTZER S., SCHMIDT C., DEWITT R. & FUCHS M. 2014. — The a-value of polymineral fine grain samples measured with the post-IR IRSL protocol. *Radiation Measurements* 69: 18-29. https://doi.org/10.1016/j.radmeas.2014.04.027

KREUTZER S., MARTIN L., GUÉRIN G., TRIBOLO C., SELVA P. & MERCIER N. 2018a. — Environmental Dose Rate Determination Using a Passive Dosimeter: Techniques and Workflow for alpha-Al_2O_3:C Chips. *Geochronometria* 45: 56-67. https://doi.org/10.1515/geochr-2015-0086

KREUTZER S., DIETZE M., BUROW C., FUCHS M. C., SCHMIDT C., FISCHER M. & FRIEDRICH J. 2018b. — Luminescence: Comprehensive Luminescence Dating Data Analysis. R package version 0.8.5. https://cran.r-project.org/package=Luminescence

KREUTZER S., MAUZ B., MARTIN L. & MERCIER N. 2019a. — 'RCarb': Dose Rate Modelling of Carbonate-Rich Samples - an Implementation of *Carb* in R -. *Ancient TL* 37 (2): 1-8. http://ancienttl.org/ATL_37-2_2019/ATL_37-2_Kreutzer_p1-8.pdf

KREUTZER S., NATHAN R. P. & MAUZ B. 2019b. — RCarb: Dose Rate Modelling of Carbonate-Rich Samples. CRAN version 0.1.4. https://CRAN.R-project.org/package=RCarb

LAI Z., ZÖLLER L., FUCHS M. & BRÜCKNER H. 2008. — Alpha efficiency determination for OSL of quartz extracted from Chinese loess. *Radiation Measurements* 43:767-770. https://doi.org/10.1016/j.radmeas.2008.01.022

LANG A. & WAGNER G. A. 1996. — Infrared Stimulated Luminescence Dating of Archaeosediments. *Archaeometry* 38: 129-141. https://doi.org/10.1111/j.1475-4754.1996.tb00766.x

LISIECKI L. E. & RAYMO M. E. 2005. — A Pliocene-Pleistocene stack of 57 globally distributed benthic $\delta^{18}O$ records. *Paleoceanography* 20: 1-17. https://doi.org/10.1029/2004PA001071

LÓPEZ-SÁEZ J. A., TEXIER P.-J. & THI MAI B. 1998. — Paléoenvironment durant le Pleistocene supérieur en Vaucluse: analyse palynologique des couches inférieures de l'abri de la Combette (Bonnieux, Vaucluse, France). *Trabajos de prehistoria* 55: 151-162. https://doi.org/10.3989/tp.1998.v55.i2.308

MARSHACK A. 1989. — Evolution of the human capacity: The symbolic evidence. *American Journal of Physical Anthropology* 32: 1-34. https://doi.org/10.1002/ajpa.1330320503

MARTI A., FOLCH A., COSTA A. & ENGWELL S. 2016. — Reconstructing the plinian and co-ignimbrite sources of large volcanic eruptions: A novel approach for the Campanian Ignimbrite. *Scientific Reports* 6: 21220. https://doi.org/10.1038/srep21220

MAUZ B. & HOFFMANN D. 2014. — What to do when carbonate replaced water: Carb, the model for estimating the dose rate of carbonate-rich samples. *Ancient TL* 32: 24-32.

MEJDAHL V. 1987. — Internal radioactivity in quartz and feldspar grains. *Ancient TL* 5: 10-17.

MELLARS P. 2004. — Neanderthals and the modern human colonization of Europe. *Nature* 432: 461-465. https://doi.org/10.1038/nature03103

MERCIER D. 2013. — *Géomorphologie de la France*. Dunod: 320 p.

MERCIER N., VALLADAS H., JORON J. L., REYSS J. L., LÉVÊQUE F. & VANDERMEERSCH B. 1991. — Thermoluminescence dating of the late Neanderthal remains from Saint-Césaire. *Nature* 351: 737-739. https://doi.org/10.1038/351737a0

MERCIER N., VALLADAS H. & VALLADAS G. 1992. — Observations on paleodose determination with burnt flints. *Ancient TL* 10: 28-32.

MESZNER S., KREUTZER S., FUCHS M. & FAUST D. 2013. — Late Pleistocene landscape dynamics in Saxony, Germany: Paleoenvironmental reconstruction using loess-paleosol sequences. *Quaternary International* 296: 95-107. https://doi.org/10.1016/j.quaint.2012.12.040

Mologni C. 2017. — *Activités humaines et changements environnementaux dans le Site Néandertalien de La Combette : une Approche micromorphologique et sédimentologique (Bonnieux, Vaucluse, France).* Mémoire de Master 2, Université de Nice Sophia-Antipolis, CEPAM, 99p.

Mologni C., Purdue L., Audiard B., Dubar M., Kreutzer S., Brochier J.-E. & Texier P.-J. (in press). — Sedimentary processes and paleoenvironments from 'La Combette' sequence (south- eastern France): climatic insights on the Last Interglacial/Glacial transition. *Palaeogeography, Palaeoclimatology, Palaeoecology*: 1-42.

Moulin F. 1904. — L'abri moustérien du Bau de l'Aubesier (Vaucluse). *Bulletin Préhistorique de France* 1 (1): 14-20. https://doi.org/10.3406/bspf.1904.11230

Murray A. S. & Wintle A. G. 2000. — Luminescence dating of quartz using an improved single-aliquot regenerative-dose protocol. *Radiation Measurements* 32: 57-73. https://doi.org/10.1016/S1350-4487(99)00253-X

Nathan R. P. & Mauz B. 2008. — On the dose-rate estimate of carbonate-rich sediments for trapped charge dating. *Radiation Measurements* 43: 14-25. https://doi.org/10.1016/j.radmeas.2007.12.012

Obreht I., Hambach U., Veres D., Zeeden C., Bösken J., Stevens T., Marković S. B., Klasen N., Brill D., Burow C. & Lehmkuhl F. 2017. — Shift of large-scale atmospheric systems over Europe during late MIS 3 and implications for Modern Human dispersal. *Scientific Reports* 7: 1-10. https://doi.org/10.1038/s41598-017-06285-x

Plummer M., Best N., Cowles K. & Vines K. 2006. — CODA: Convergence Diagnosis and Output Analysis for MCMC. *R News* 6: 7-11.

Prescott J. R. & Hutton J. T. 1994. — Cosmic ray contributions to dose rates for luminescence and ESR dating: Large depths and long-term time variations. *Radiation Measurements* 23: 497-500. https://doi.org/10.1016/1350-4487(94)90086-8

Preusser F., Degering D., Fuchs M., Hilgers A., kadereit A., Klasen N., Krbetschek M. R., Richter D. & Spencer J. Q. G. 2008. — Luminescence dating: basics, methods and applications. *Eiszeitalter und Gegenwart (Quaternary Science Journal)* 57: 95-149. https://doi.org/10.3285/eg.57.1-2.5

R Core Team 2019. — R: A Language and Environment for Statistical Computing. *R Foundation for Statistical Computing,* Vienna, Austria. https://www.r-project.org.

Richter D., Mercier N., Valladas H., Jaubert J., Texier P. J., Brugal J. P., Kervazo B., Reyss J. L., Joron J. L. & Wagner G. A. 2007. — Thermoluminescence dating of heated flint from the Mousterian site of Bérigoule, Murs, Vaucluse, France. *Journal of Archaeological Science* 34: 532-539. https://doi.org/10.1016/j.jas.2006.06.006

Richter D., Richter A. & Dornich K. 2015. — Lexsyg smart — a luminescence detection system for dosimetry, material research and dating application. *Geochronometria* 42: 202-209. https://doi.org/10.1515/geochr-2015-0022

Rink W. J. 1997. — Electron spin resonance (ESR) dating and ESR applications in quaternary science and archaeometry. *Radiation Measurements* 27: 975-1025. https://doi.org/10.1016/S1350-4487(97)00219-9

Roberts H. M. 2008. — The development and application of luminescence dating to loess deposits: a perspective on the past, present and future. *Boreas* 37: 483-507. https://doi.org/10.1111/j.1502-3885.2008.00057.x

Rousseau D. D., Derbyshire E., Antoine P. & Hatté C. 2007. — LOESS RECORDS | Europe *in* Elias S. A. (ed.), *Encyclopedia of Quaternary Science*. Elsevier: 1440-1456. https://doi.org/10.1016/B0-44-452747-8/00162-9

Rousseau D. D. & Sima A. 2014. — Abrupt climate changes recorded in loess sequences. *Pages Magazine* 22: 30-31. https://doi.org/10.1029/2007GL031716/abstract

Schmidt C., Pettke T., Preusser F., Rufer D., Kasper H. U. & Hilgers A. 2012. — Quantification and spatial distribution of dose rate relevant elements in silex used for luminescence dating. *Quaternary Geochronology* 12: 65-73. https://doi.org/10.1016/j.quageo.2012.05.006

Schmidt C., Rufer D., Preusser F., Krbetschek M. & Hilgers A. 2013. — The Assessment of Radionuclide Distribution in Silex By Autoradiography in the Context of Dose Rate Determination for Thermoluminescence Dating. *Archaeometry* 55: 407-422. https://doi.org/10.1111/j.1475-4754.2012.00690.x

Selo M., Valladas H., Mercier N., Joron J. L., Bassinot F., Person A. & Nouet J. 2009. — Investigations of uranium distribution in flints. *Radiation Measurements* 44: 615-619. https://doi.org/10.1016/j.radmeas.2009.03.004

Shepard F. P. 1954. — Nomenclature Based on Sand-silt-clay Ratios. *Journal of Sedimentary Petrology* 24: 151-158.

Smedley R. K., Duller G. A. T., Pearce N. J. G. & Roberts H. M. 2012. — Determining the K-content of single-grains of feldspar for luminescence dating. *Radiation Measurements* 47: 790-796. https://doi.org/10.1016/j.radmeas.2012.01.014

Texier P.-J. 2004a. — L'abri du pont de la Combette (Bonnieux, Vaucluse), *in* Poster presentation, *Centenaire de la Société Préhistorique Française, XXVI^e congrès, Avignon-Bonnieux, September 2004*. https://doi.org/10.13140/RG.2.1.2774.1844

Texier P.-J. 2004b. — Le Paléolithique moyen de la Montagne du Luberon au Mont Ventoux, *in* Barthélemy A. (ed.), *Vaucluse Préhistorique : Le territoire, Les hommes, les cultures et les sites*. Ministère de la Culture et de la Communication, Le Pontet: 61-92.

Texier P.-J., Brugal J.-P., Desclaux E., Lemorini C., Sáez J. A. L., Thery I. & Wilson L. 2003. — La Combette (Bonnieux, Vaucluse, France): a Mousterian sequence in the Luberon mountain chain, between the plains of the Durance and Calavon rivers. *Preistoria Alpina* 39: 77-90.

Texier P.-J., Brugal J. P., Lemorini C., Lopez-Saez J. A., Thery I., Valladas H. & Wilson L. 2002. — L'abri de la Combette site paléolithique moyen à Bonnieux (Vaucluse). Rapport de fin fouille 1989-2002 (unpublished report).

Texier P.-J., Lemorini C., Brugal J. P. & Wilson L. 1996. — Une activité de traitement des peaux dans l'habitat moustérien de la Combette (Bonnieux, Vaucluse, France). *Quaternaria Nova* VI: 369-392.

Théry-Parisot I. & Texier P.-J. 2006. — La collecte du bois de feu dans le site moustérien de la Combette (Bonnieux, Vaucluse, France) : implications paléo-économiques et paléo-écologiques. Approche morphométrique des charbons de bois*). Bulletin de la Société préhistorique française* 103: 453-463. https://doi.org/10.3406/bspf.2006.13466

Thomsen K. J., Murray A. S., Jain M. & Bøtter-Jensen L. 2008. — Laboratory fading rates of various luminescence signals from feldspar-rich sediment extracts. *Radiation Measurements* 43: 1474-1486. https://doi.org/10.1016/j.radmeas.2008.06.002

Tribolo C., Kreutzer S. & Mercier N. 2019. — How reliable are our beta-source calibrations? *Ancient TL* 37: 1-10.

Valladas G. 1978. — A gamma ray irradiator, *PACT 3 - Revue du Réseau Européen de Sciences et Techniques appliquées au Patrimoine Culturel*: 439-442.

Valladas H. 1985. — *Datation par la thermoluminescence de gisements moustériens du Sud de la France*. Unpublished PhD thesis, Université Paris VI, Paris.

Valladas G. 1987. — A gamma-ray irradiator. *PACT* 3: 439-442.

Valladas G. & Valladas G. 1982. — Effet de l'irradiation alpha sur des grains de quartz. *PACT* 6: 171-178.

Valladas G., Mercier N. & Létuvé R. 1994. — A simple semi-automatic TL apparatus of new design. *Ancient TL* 12: 39-40.

Vandenberghe D., De Corte F., Buylaert J. P., Kučera J. & Van den haute P. 2008. — On the internal radioactivity in quartz. *Radiation Measurements* 43: 771-775. https://doi.org/10.1016/j.radmeas.2008.01.016

WAGNER G. A., WALTER R. & LANG A. 2002. — Thermoluminescence and ESR dating of the Palaeolithic site La Combette (Vaucluse), *in* TEXIER P.-J., BRUGAL J. P., LEMORINI C., LOPEZ-SAEZ J. A., THERY I., VALLADAS H. & WILSON L. (eds), *L'abri de la Combette Site Paleolithique moyen à Bonnieux Vaucluse*: 108-111 (*unpublished report*).
WALTHER R. 1995. — *Elektronen-Spin-Resonanz-Datierung an Silikaten. Grundlagen, Systematik und Anwendung am Beispiel von Quarzen und Feuerstein. Anwendung am Beispiel von Quarzen und Feuersteinen*. PhD thesis (in German), Heidelberg University, Heidelberg, 100 p.
WALTHER R. & ZILLES D. 1994. — ESR studies on flint with a difference-spectrum method. *Quaternary Science Reviews* 13: 635-639. https://doi.org/10.1016/0277-3791(94)90091-4
WICKHAM H. 2016. — *ggplot2: Elegant Graphics for Data Analysis*. Springer-Verlag New York.
WINTLE A. G. 1973. — Anomalous Fading of Thermoluminescence in Mineral Samples. *Nature* 245 (5421): 143-144. https://doi.org/10.1038/245143a0
ZIMMERMAN D. W. 1971. — Thermoluminescent dating using fine grains from pottery. *Archaeometry* 13: 29-52. https://doi.org/10.1111/j.1475-4754.1971.tb00028.x
ZÖLLER L. 2010. — New approaches to European loess: a stratigraphic and methodical review of the past decade. *Central European Journal of Geosciences* 2: 19-31. https://doi.org/10.2478/v10085-009-0047-y
ZÖLLER L. & SEMMEL A. 2001. — 175 years of loess research in Germany - long records and "unconformities. *Earth-Science Reviews* 54: 19-28. https://doi.org/10.1016/S0012-8252(01)00039-3

Submitted on 26 September 2019;
accepted on 31 March 2020;
published on 7 April 2021.

APPENDICES

APPENDIX 1. — Granulometry.

For the six sediment samples taken in 2014, granulometric measurements were carriedout at the PACEA (Université de Bordeaux) using a Horiba LA-950 laser particle size analyser (cf. Bosq *et al.* 2018, see Material and methods). Figures and brief interpretations of the results are given in the following. To unmix the grain-size distributions we applied the R package "EMMAgeo" (Dietze *et al.* 2012; Dietze & Dietze 2019a, b) (Appendix 4). For the analysis we followed the suggestions of the "compact protocol" according to Dietze & Dietze (2019a, their fig. 1 and supplement; slightly modified):

```
## X contains the grain size analysis data imported
## previously into R

## check data
check.data(X = X,
           q = 4,
           l = 0,
           c = 100)

## get range of l
 l <- get.l(X)

## get q_min and q_max
q <- get.q(X, l = l)

## run all possible models
EM_pot <- model.EM(X, q = q, l = l, plot = FALSE)

## get or set mode limits
limits <- get.limits(loadings = EM_pot)

## extract robust end-members
robust.EM(
  EM_pot,
  limits = limits,
  plot = TRUE,
  ID = rownames(X),
  classunits = as.numeric(colnames(X)),
  xlab = c("Grain size class [µm]", "Sample ID")
 )
```

Please note that, however, this approach must remain superficial due to the small amount of samples (here six) used for the end-member modelling.

Appendix 2. — Granulometric histogram of all samples. While four samples (BDX16811 to BDX16814) are dominated by silt, the two lowermost samples (cf. profile graph in the main text) comprise a dominating sand component. The figure was produced using the R package "rysgran" (Gilbert *et al.* 2014).

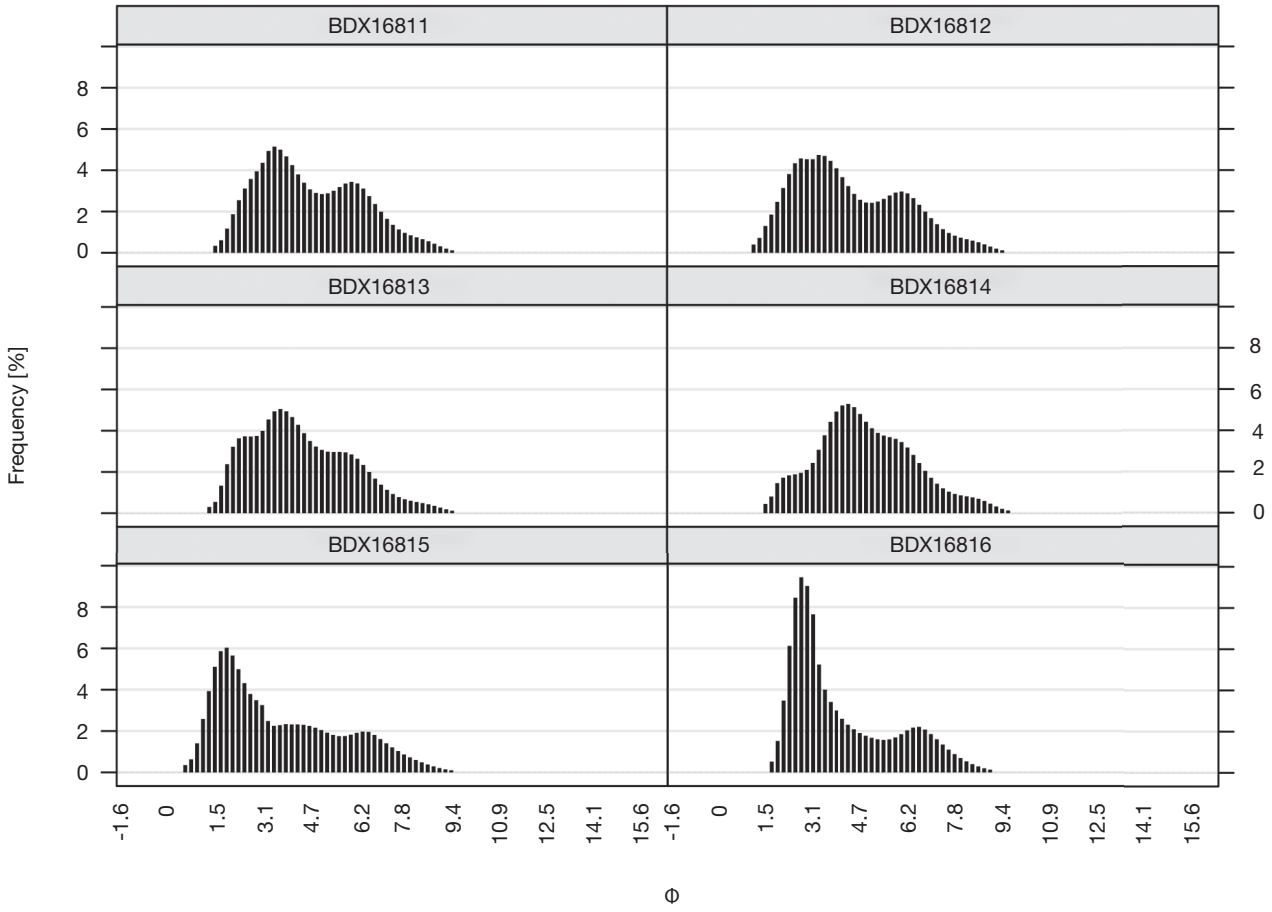

APPENDIX 3. —Ternary diagram showing granulometric classes of the samples according to Shepard (1954). Three out of six samples are dominated by sandy silt, while the other three samples are dominated by silty sand. The figure was produced using the R package 'rysgran' (Gilbert *et al.* 2014).

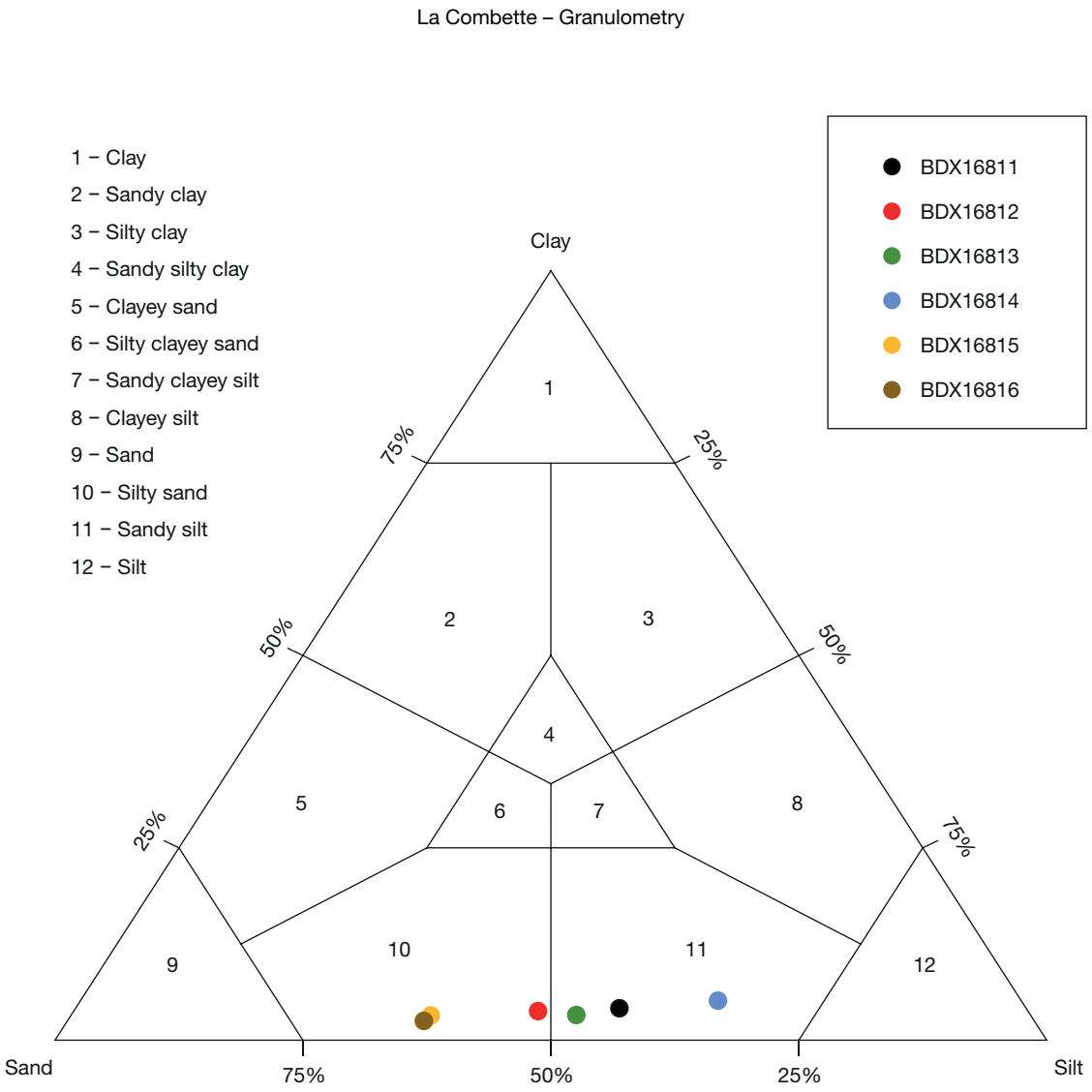

Appendix 4. — The graphic displays end-member modelling results returned by the R package "EMMAgeo" (Dietze & Dietze 2019b). The end-member loadings show that three main processes dominated the sediment accumulation of the loess sequence: **1**, aeolian; **2**, fluvial; and **3**, gravimetric, probably fluvial dominated, transport processes. The bottom-right figure shows that the lowermost two samples are dominated by high-energy fluvial transport processes, while the upper four samples are of aeolian and fluvial origin.

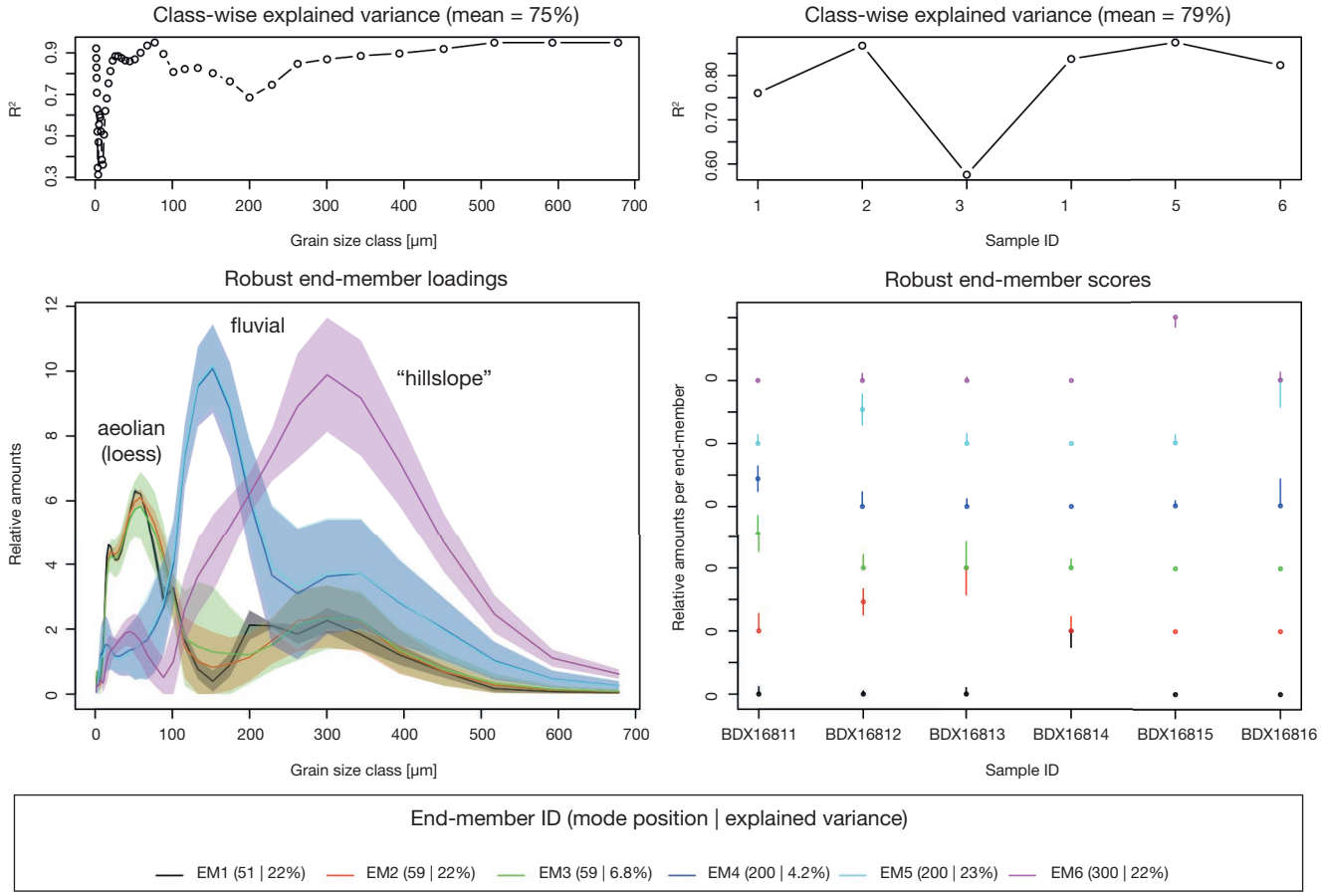

APPENDIX 5. — Additional information luminescence dating.

DETAILS MEASUREMENT PROTOCOL SETTINGS

All measurements were carried out in N_2 atmosphere. The below listed protocols have been used consistently for all samples.

SAR PROTOCOL (QUARTZ FRACTION)

For all measurements, the preheats were recorded as TL measurement with an additional neutral density filter (ND 0.1) attached in front of the PMT to avoid a signal oversaturation. The channel resolution for the OSL measurements was set to 0.1 s/channel. Chosen integral channel limits were 1-3 for the signal, and 800-999 for the background. The dose points were best fit with an exponential + linear function. Applied rejection criteria: Recycling ratio: max. ± 10%, recuperation rate: max. 10%, test dose error: max. 10%, and palaeodose error: max. 10%. We found no significant feldspar contamination (noise like IRSL tests curves) or initial IRSL signals <= 2% compared to the corresponding green OSL signal.

$pIRIR_{225}$ PROTOCOL (POLYMINERAL FRACTION)

The channel resolution was set to 0.1 s/channel. In contrast to the OSL SAR measurements, the preheats were not recorded as TL. For the polymineral samples only the $pIRIR_{225}$ signal was used to estimate the D_e. Chosen integral channel limits were 1-3 for the signal, and 800-999 for the background. The dose points were fitted with a single exponential function.

β -SOURCE CALIBRATION

The inbuilt β-source used for the irradiation of the sediment samples (OSL and pIRIRI225), was calibrated using a coastal dune quartz sample (BDX16651) from the Medoc area (south-west France). The sample was first gently crushed and the grain size fraction of 4-11 µm was extracted by applying the Stokes' law. Before irradiation, the material was heated to 700°C in air and additionally tested for feldspar contamination using IRSL. Two batches of the sample were shipped for irradiation to the Gif-sur-Yvette laboratory. A third control batch was kept in Bordeaux. The two shipped batches received a γ-dose of 2.5 Gy (rel. SE: 3%) and 5 Gy (rel. SE: 3%), while the third batch was never irradiated. The irradiation was carried out using a homemade irradiator equipped with a ^{137}Cs γ-source (Valladas 1987). The source is a ring consisting of six single circularly arranged ^{137}Cs γ-sources. The sample is placed in the middle.

All three batches were measured and the source-dose rate was deduced from the slope of the regression line of the measured vs the given dose. The so obtained source-dose rate (0.155 ± 0.004 Gy s^{-1} at the calibration date) of the quartz fine grain fraction is *c*. 13% lower than the corresponding source dose rate of quartz coarse (100-200 µm) grain quartz (0.178 ± 0.0006 Gy s^{-1}) on the same reader. This grain size related deviation in the source-dose rate is in accordance with the results reported by Armitage & Bailey (2005).

DRAC MODIFICATIONS

For the age calculation we used the freely available software DRAC (Durcan *et al.* 2015). DRAC applies the water correction factors by Zimmerman (1971) and Aitken & Xie (1990). However, given the high calcium carbonate concentration at La Combette, we modified these values for a calcium carbonate concentration of 20% and a water content of 5% in accordance with data published by Nathan & Mauz (2008) (β-radiation, γ-radiation) and Kreutzer *et al.* (2019a) (α-radiation). The modification in the PHP code concerned a single line in the file calculator=lookup tables:php as shown below:

Original code line lookup tables.php

```
248 | $drac_LT5 = array( 'Alpha' => 1.49, 'Beta' => 1.25, 'Gamma' => 1.14, );
```

Modified code line lookup_tables.php

```
248 | $drac_LT5 = array( 'Alpha' => 1.49, 'Beta' => 1.25, 'Gamma' => 1.14, );
```

The modified version of DRAC was run on a local server.

AGE CALCULATION

For the used DRAC settings please see Appendix 8. Additional, the full DRAC input and output dataset is provided as CSV-file, including the re-calculated age results based on data given in Wagner *et al.* (2002). The final ages include systematic uncertainties for $\dot{D}_\alpha$ (1%), $\dot{D}_\beta$ (1%), $\dot{D}_\gamma$ (5%) (both for dosimeter and γ-ray spectrometry measurements), and for the ^{90}Sr/^{90}Y source-calibration (3%). No information on the systematic uncertainty contribution was available for the ages by Wagner *et al.* (2002).

For the flint samples, we assumed a systematic error of 10% for each radioelement (U, Th, K) determined by NAA. A 2% systematic error was applied to the doses delivered by the radioactive sources.

RESULTS DOSE-RATE MODELLING USING 'RCarb'

The potential CaCO3 cementation process was modelled using the R package 'RCarb' (Kreutzer *et al.* 2019b). Below we list the relevant R function call. We provide input and output tables as CSV-files along with this supplement.

```
temp <- read.table(file.choose())

results <- model_DoseRate(
  temp[1:4, ],
  DR_conv_factors = "Guerin_et_al_2011",
  n.MC = 100,
  par_local = FALSE
)
```

Appendix 6. — SAR protocol used for measuring the fine grain quartz fraction. (*) Dose points: (0, 54.3, 116.3, 193.8, 217.3, 0, 54.3) Gy. OSL stimulation power density: 50 mW cm^{-2}; all OSL steps included a temperature stabilisation phase of 10 s.

Step	Description	Signal
1	Irradiation*	–
2	Preheat as TL to 220°C for 10 s	–
3	OSL for 100 s at 125°C	L_x
4	Irradiation (11.6 Gy)	–
5	Preheat as TL to 180°C for 10 s	–
6	OSL for 100 s at 125°C	T_x
7	Hotbleach (OSL) for 100 s at 280°C	–

Appendix 7. — Post-IR IRSL protocol used for measuring the polymineral fraction. (*) Dose points: {0, 38.8, 155, 232.5, 387.5, 0 , 38.8} Gy; for preliminary tests, we recorded dose-response curves without zero dose and recycled dose point. IRSL stimulation power density: 12 0mW cm^{-2}, the $pIRIR_{225}$ step included a temperature stabilisation phase of 15 s.

Step	Description	Signal
1	Irradiation*	–
2	Preheat to 250°C for 60 s	–
3	IRSL for 100 s at 50°C	IR_{50}-L_x
4	IRSL for 100 s at 225°C	$pIRIR_{225}$-L_x
5	Irradiation (12.4 Gy)	–
6	Preheat to 250°C for 60 s	–
7	IRSL for 100 s at 50°C	IR_{50}-T_x
8	IRSL for 100 s at 225°C	$pIRIR_{225}$-T_x

Appendix 8. — DRAC settings applied for the luminescence age calculation. For details on the meaning of the parameters, we refer to the online reference manual of DRAC.

Parameter	DRAC input	Reference
Dose rate conversion factors	Guerinetal2011	Guérin *et al.* (2011)
Cal. external Rb from K conc?	Y	Mejdahl (1987)
Internal U (ppm)	0.08 | 0.02	Vandenberghe *et al.* (2008)
Internal Th (ppm)	0.18 | 0.03	Vandenberghe *et al.* (2008)
Internal K (%)	10.0 | 2.0	Smedley *et al.* (2012)
β-grain size attenuation	Guerinetal2012-F	Guérin *et al.* (2012)
α-grain size attenuation	Brennanetal1991	Brennan *et al.* (1991)
Water content	5.0 | 2.5	Prescott & Hutton (1994)
Cosmic-dose rate	43.8 | 5.3 | 327.0	Prescott & Hutton (1994)

Appendix 9. — Preheat plateau tests (**A**) and preheat dose-recovery test (**B**) performed to determine the SAR protocol parameters for the quartz samples. Show are results for the samples BDX16811 and BDX16814 (**A**) and results for samples BDX16811 to BDX16814 (**B**). For a better visibility, the results are summarised as boxplots, each boxplot representing the results of three aliquots. For the final measurements, a preheat – cutheat combination of 220°C and 180°C was chosen. In figure **B**, sample BDX16811 shows extreme values, significantly overestimating the given dose. For this sample, we observed that the recycling ratios always exceed the set threshold of 10%. However, this behaviour could not be reproduced in subsequent D_e measurements after the sample was etched another time in H_2SiF_6. The results here are displayed for the matter of completeness.

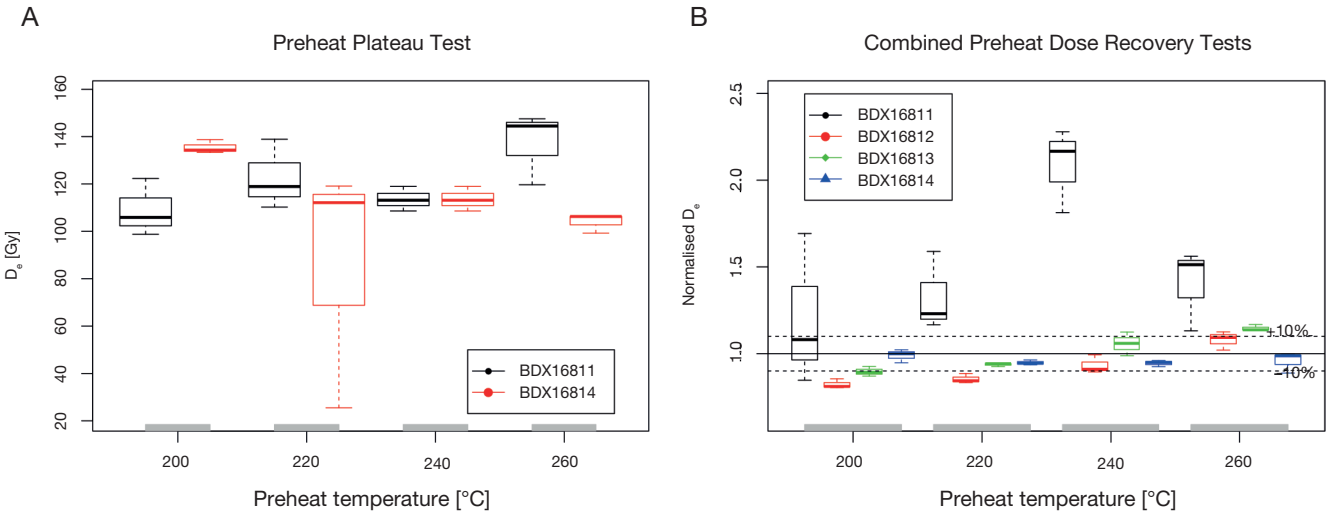

APPENDIX 10. — Kernel density plots of the D_e distribution derived from the $pIRIR_{225}$ signal of the polymineral fraction. Please note that for samples BDX16811 to BDX16814 the plots show the results of the pretests. For those measurements, no zero dose and no recycled dose points were recorded.

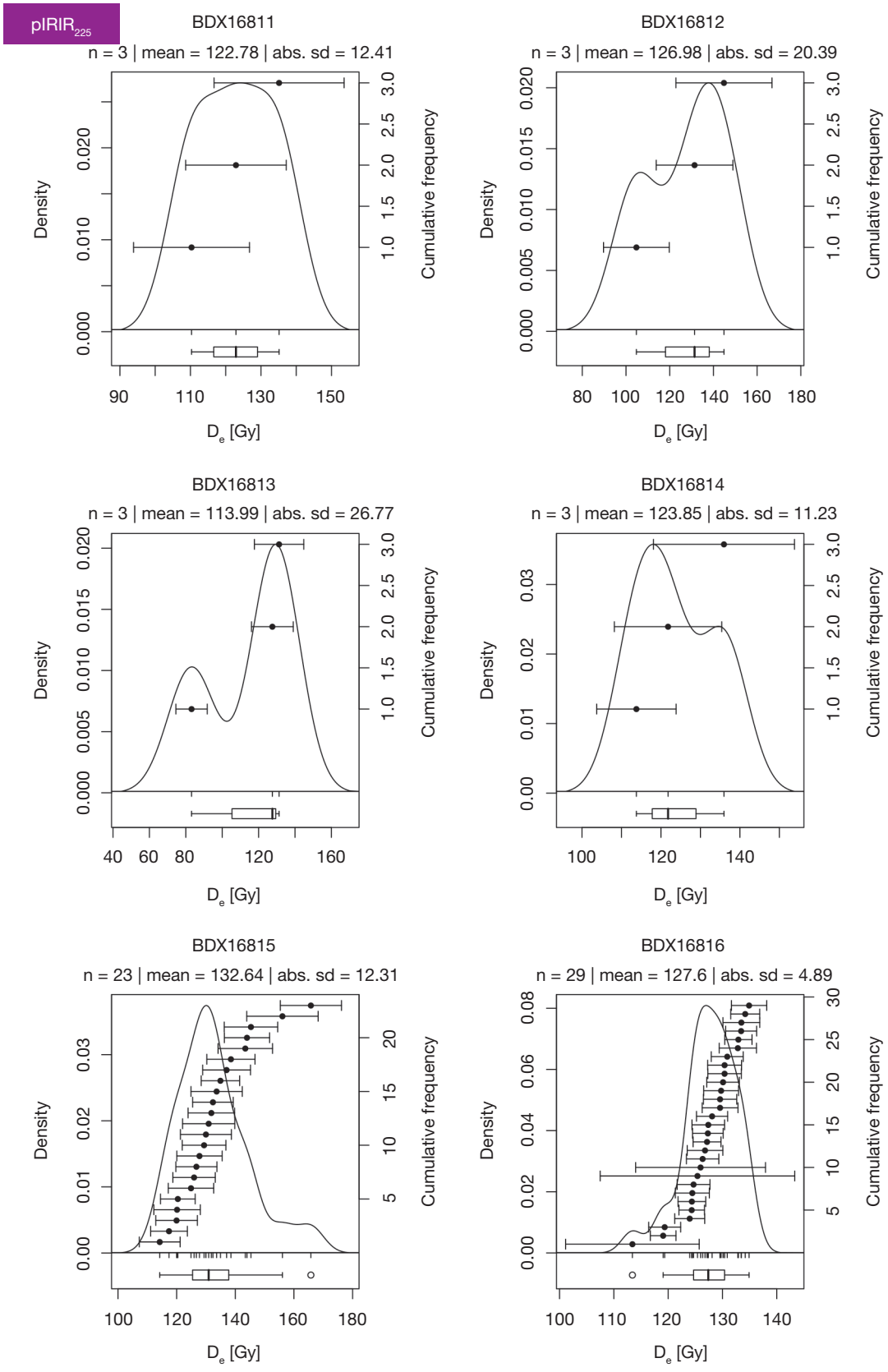

Appendix 11. — Dosimetric results silex samples. Abbreviations: **int**, internal; **cosm**, cosmic; **ext**, external.

	INTERNAL NUCLIDE CONC.							
ID	U [ppm]	Th [ppm]	K [%]	S_α [μGy/(10³α cm⁻²)]	$\dot{D}_{int}$ [Gy ka⁻¹]	$\dot{D}_{cosm}$ [Gy ka⁻¹]	$\dot{D}_{ext}$ [Gy ka⁻¹]	$\dot{D}_{total}$ [Gy ka⁻¹]
LC01	0.32 ± 0.032	0.038 ± 0.004	0.038 ± 0.002	25.96 ± 1.04	0.21 ± 0.02	0.12 ± 0.02	0.27 ± 0.03	0.49 ± 0.03
LC03	0.177 ± 0.018	0.084 ± 0.008	0.084 ± 0.003	23.42 ± 3.04	0.13 ± 0.01	0.12 ± 0.01	0.28 ± 0.03	0.4 ± 0.03
LC04	0.82 ± 0.082	0.073 ± 0.007	0.073 ± 0.004	22.14 ± 4.21	0.48 ± 0.07	0.12 ± 0.01	0.63 ± 0.05	1.11 ± 0.08
LC05	0.82 ± 0.082	0.115 ± 0.012	0.115 ± 0.004	19.2 ± 1.15	0.44 ± 0.03	0.14 ± 0.01	0.56 ± 0.04	1 ± 0.05
LC07	0.82 ± 0.082	0.04 ± 0.004	0.04 ± 0.002	22.18 ± 2.22	0.45 ± 0.04	0.15 ± 0.02	0.6 ± 0.04	1.05 ± 0.06
LC08	1.42 ± 0.142	0.055 ± 0.006	0.055 ± 0.003	25.4 ± 1.27	0.86 ± 0.07	0.14 ± 0.01	0.57 ± 0.05	1.43 ± 0.08
LC09	0.16 ± 0.016	0.009 ± 0.001	0.009 ± 0.001	24.28 ± 0.97	0.1 ± 0.01	0.1 ± 0.01	0.53 ± 0.04	0.63 ± 0.05
LC12	0.96 ± 0.096	0.176 ± 0.018	0.176 ± 0.002	8.63 ± 0.26	0.31 ± 0.02	0.12 ± 0.01	0.45 ± 0.03	0.76 ± 0.03
LC15	0.069 ± 0.007	0.021 ± 0.002	0.021 ± 0.001	16.82 ± 1.35	0.04 ± 0	0.1 ± 0.01	0.57 ± 0.05	0.61 ± 0.05
LC16	3.51 ± 0.351	0.069 ± 0.007	0.069 ± 0.003	24.65 ± 2.22	2.04 ± 0.2	0.09 ± 0.01	0.36 ± 0.03	2.4 ± 0.2
LC17	1.02 ± 0.102	0.047 ± 0.005	0.047 ± 0.001	11.68 ± 0.35	0.37 ± 0.03	0.08 ± 0.01	0.43 ± 0.02	0.8 ± 0.03
LC19	3.44 ± 0.344	0.018 ± 0.002	0.018 ± 0.002	17.74 ± 0.89	1.58 ± 0.13	0.08 ± 0.02	0.43 ± 0.02	2.01 ± 0.13
LC21	0.47 ± 0.047	0.108 ± 0.011	0.108 ± 0.003	24.06 ± 1.44	0.3 ± 0.02	0.13 ± 0.01	0.56 ± 0.04	0.86 ± 0.05
LC22	1.03 ± 0.047	0.003 ± 0.011	0.003 ± 0.003	12.16 ± 0.97	0.38 ± 0.02	0.09 ± 0.01	0.58 ± 0.05	0.95 ± 0.05
LC23	0.89 ± 0.103	0.141 ± 0	0.141 ± 0.001	22.2 ± 0.67	0.53 ± 0.04	0.16 ± 0.02	0.5 ± 0.14	1.03 ± 0.14
LC24	1.19 ± 0.119	0.111 ± 0.011	0.111 ± 0.003	21.6 ± 0.43	0.65 ± 0.05	0.1 ± 0.01	0.43 ± 0.03	1.08 ± 0.06
LC25	0.18 ± 0.119	0.142 ± 0.011	0.142 ± 0.003	16.7 ± 1.5	0.11 ± 0.04	0.08 ± 0.01	0.44 ± 0.02	0.55 ± 0.04
LC26	0.083 ± 0.119	0.26 ± 0.011	0.26 ± 0.003	16.8 ± 1.51	0.12 ± 0.04	0.12 ± 0.01	0.56 ± 0.04	0.69 ± 0.06
LC27	1.24 ± 0.119	0.104 ± 0.011	0.104 ± 0.003	29.19 ± 1.17	0.84 ± 0.07	0.08 ± 0.01	0.44 ± 0.02	1.28 ± 0.07
LC28	2.67 ± 0.119	0.095 ± 0.011	0.095 ± 0.003	23.61 ± 1.18	1.5 ± 0.07	0.1 ± 0.01	0.42 ± 0.03	1.93 ± 0.08
LC29	0.91 ± 0.119	0.004 ± 0.011	0.004 ± 0.003	16.8 ± 2.86	0.41 ± 0.06	0.13 ± 0.01	0.49 ± 0.07	0.9 ± 0.09
LC30	0.58 ± 0.119	0.08 ± 0.011	0.08 ± 0.003	16.93 ± 0.85	0.28 ± 0.04	0.09 ± 0.01	0.58 ± 0.05	0.86 ± 0.06
LC31	1.87 ± 0.119	0.083 ± 0.011	0.083 ± 0.003	24.27 ± 0.97	1.08 ± 0.06	0.08 ± 0.01	0.44 ± 0.02	1.52 ± 0.06
LC32	3.78 ± 0.378	0.019 ± 0.002	0.019 ± 0.001	18.52 ± 0.56	1.77 ± 0.14	0.08 ± 0.01	0.44 ± 0.02	2.21 ± 0.14

Appendix 12. — Isochron plot of the burnt flint TL data. The plot assumes that all measured artefacts from one horizon represent a similar age and the differences in the De relates to the internal dose rate only. **Black circles** display values from the archaeological layer E, and red triangles show values from the layer F/G. Dashed lines show the regression line for level E (**black**) and level F/G (**red**). The closer the values vary around the regression lines, the more likely our assumption becomes that the samples represent a similar context age. The slope of the regression lines represents the corresponding age. Quoted uncertainties are standard errors from the regression, i.e., the average distance of the data points to the regression line.

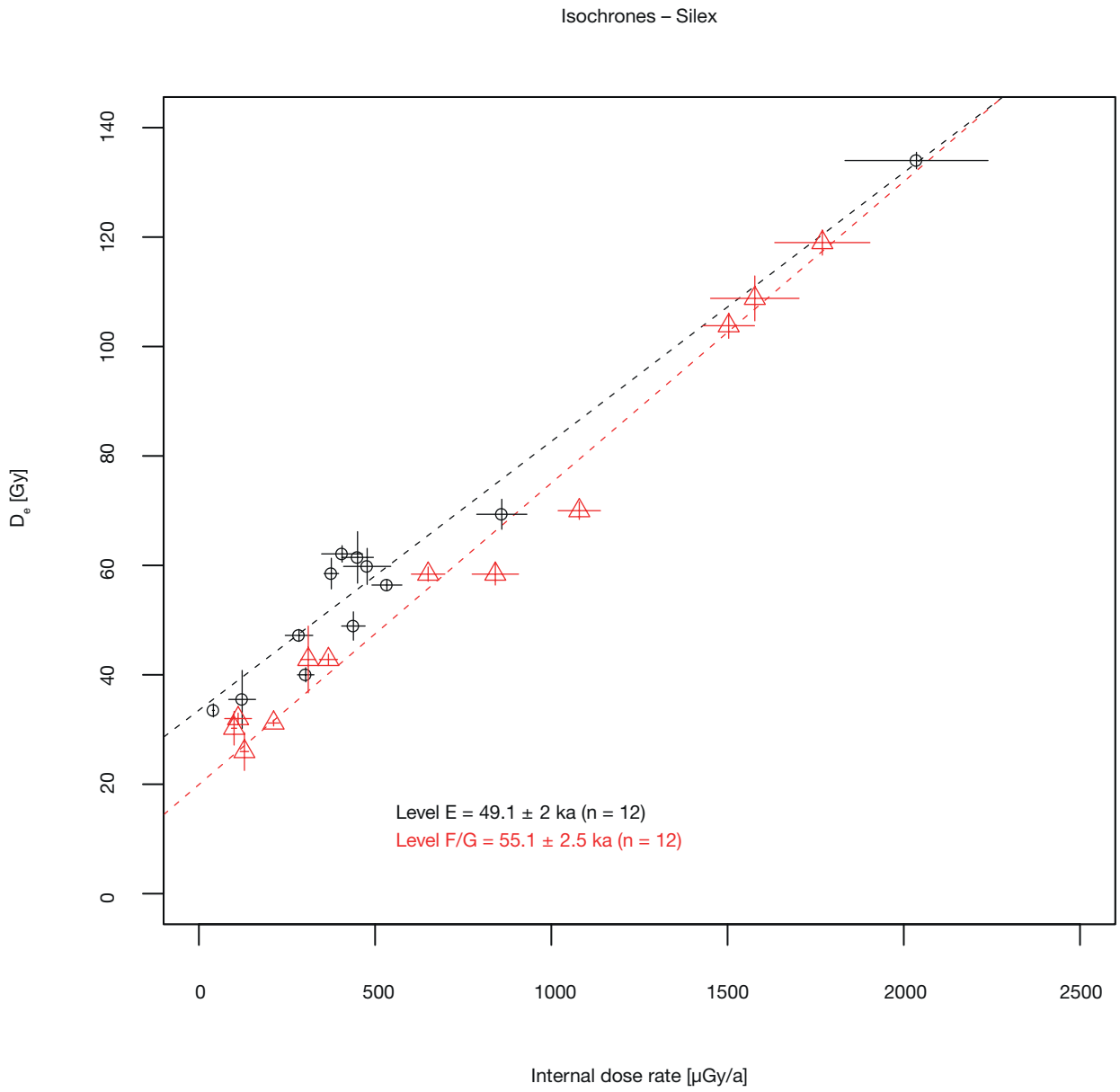

APPENDIX 13. — 'RCarb' (Kreutzer *et al.* 2019b) modelling results for the four uppermost samples of the profile La Combette. The left plots show the dose-rate evolution over time, the right plots the modelled luminescence ages. Please note that age values displayed in the plots, do include the α-dose rate contribution, these values were added manually using the α-dose rate returned by DRAC. The calculated results are part of the CSV-file attached to this supplement.

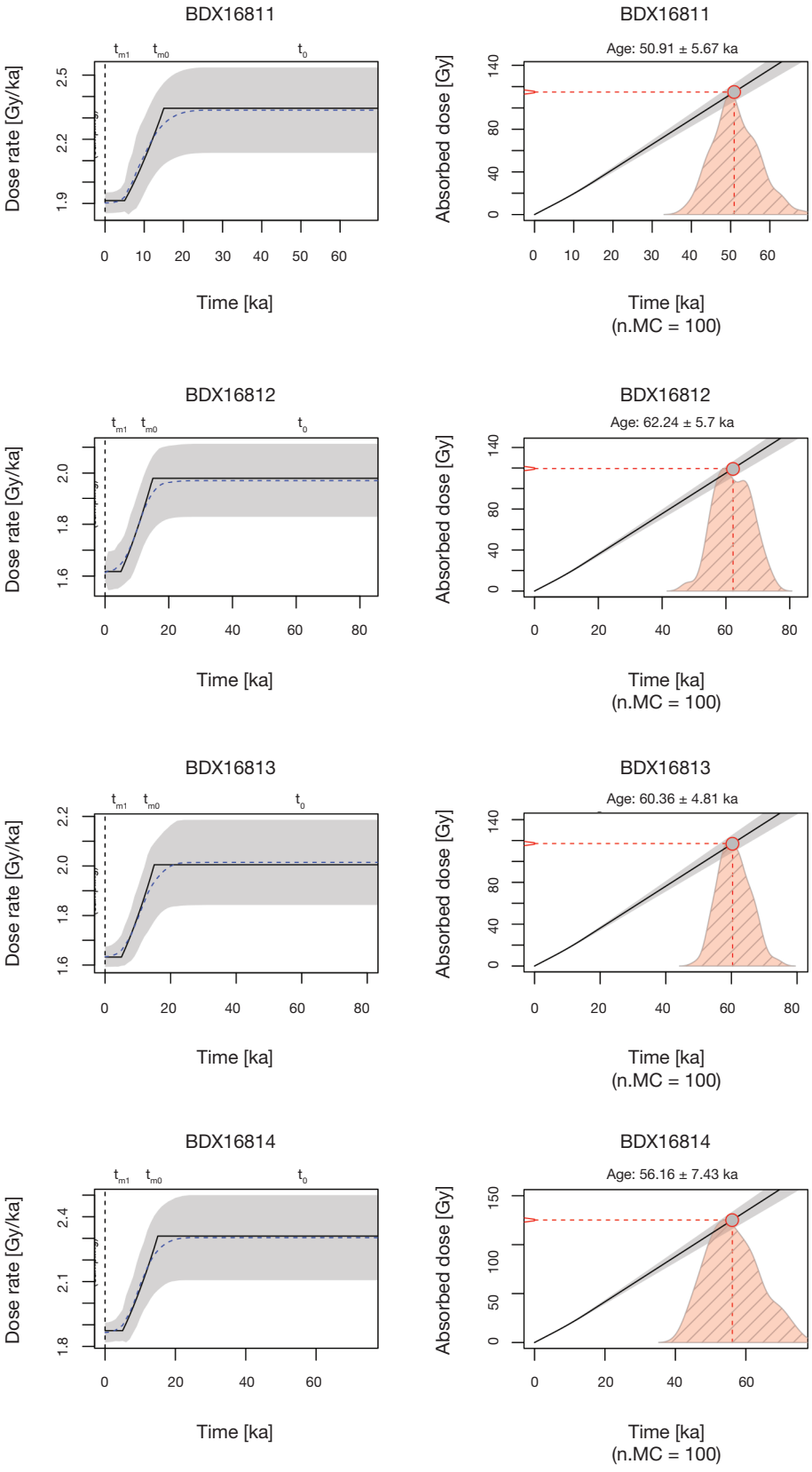

Appendix 14. — Comparison of age density distributions (see also Fig. 7 main text) for three different age calculation scenarios: **1**, the γ-dose rate was deduced from the in situ measurements and an average of 0.51 ± 0.02 Gy ka^{-1} was taken for samples where no value was measured in situ (see main text); **2**, the γ-dose rate was calculated based on measured U, Th, K concentrations; **3**, this scenario bases on scenario 1, but the four uppermost OSL ages were calculated using 'RCarb'. In summary, all three scenarios lead to a similar age interpretation. In case of scenario 3 the significant shift of the uppermost four samples of the profile towards younger ages has a negligible impact on the density distribution.

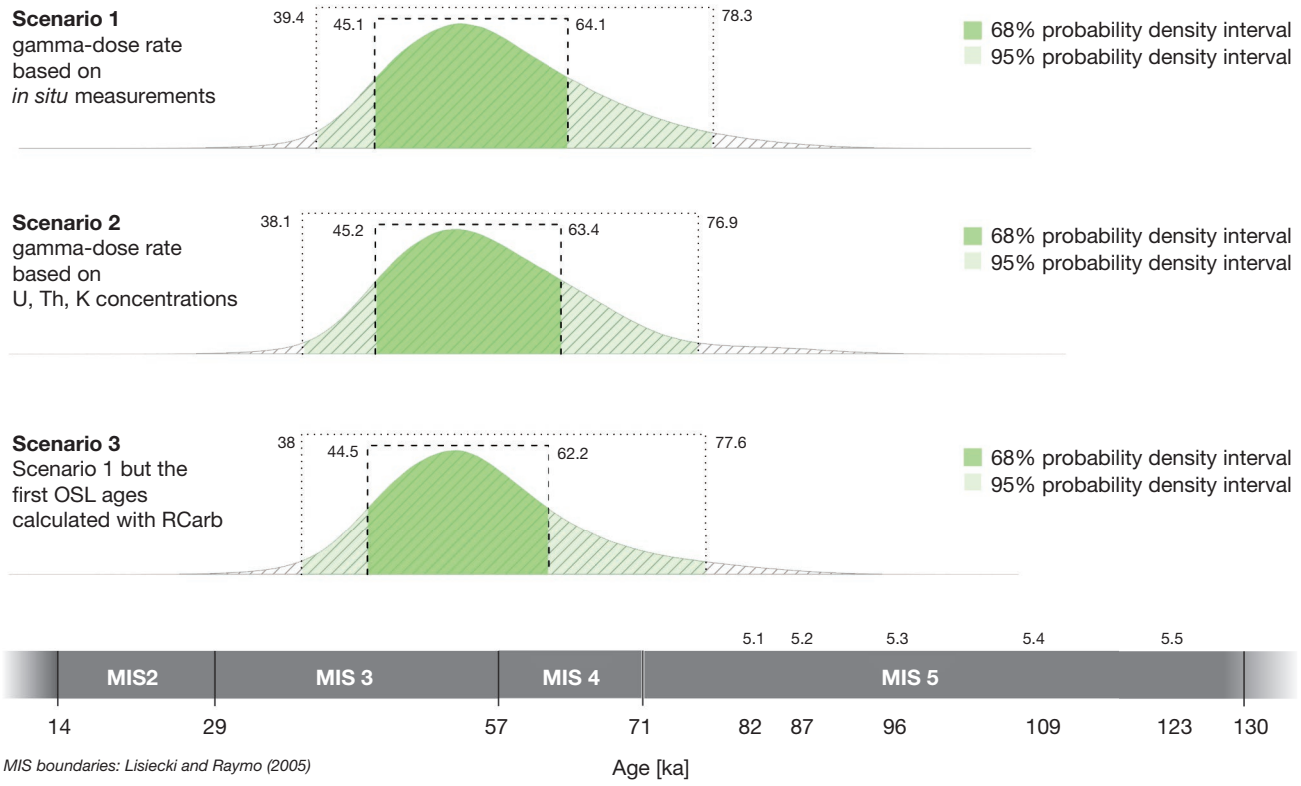

Appendix 15. — DRAC input table (CSV-file): https://doi.org/10.5852/cr-palevol2021v20a14_s1 (available here).

Appendix 16. — DRAC input table (CSV-file) used for 'RCarb' modelling: https://doi.org/10.5852/cr-palevol2021v20a14_s2 (available here).